

LEBEDEV INSTITUTE REPORT No. SLPI-1/95

Unlimited Release

Printed March 1995



FULLERENES FILM IR DETECTORS

Dityatyev A.A., Gurey A.E., Mazaev A.A., Semenov O.G., Tikhomirov A.A.

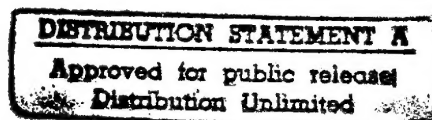
Prepared by

SEMCO PSP Ltd. and Lebedev Physics Institute

117924, Leninskii prospect 53

Moscow, Russia

for the European Office of Aerospace Research and Development
under Contract No.



19950629 013

DTIC QUALITY INSPECTED 8

ABSTRACT

On the base of analysis of experimental results and theoretic researches the phenomenological model of a charge carrier generation under the action of irradiation is presented, and the carrier transport in thin film photoadvices is discussed. A possibility of IR- sensible devices realization on the base of high fullerenes or doped fullerenes is considered. It is proposed to study Shottky transition and heterojunction with polymers for realization of all photosensitive properties of fullerenes. On the base of extended Huckel model the numeric calculations of electron structure of high fullerenes and the search of isomers with defined band gap value are made. Experimental researches of absorption spectra for UV-, optic and IR- bands are made.

Accession For	
NTIS CRA&I	<input checked="" type="checkbox"/>
DTIC TAB	<input type="checkbox"/>
Unannounced	<input type="checkbox"/>
Justification	
By	
Distribution /	
Availability Codes	
Dist	Avail and/or Special
A-1	

CONTENTS

INTRODUCTION	4
I. C ₆₀ FILM PHOTODETECTOR PHENOMENOLOGY	5
II. HUCKEL TREATMENT OF HIGH FULLERENES FOR THE CALCULATION OF BAND GAP	36
III. OPTICAL AND INFRARED SPECTROSCOPY OF FULLERENES	59

INTRODUCTION

Considerable interest exists in properties, and possible applications of fullerenes, with particular focus on the electrical properties of C_{60} films. Photophysical properties including UV-, visible absorption, photoluminescence and photoconductivity have already been reported [1,2]. Photoconductive properties are intensively studied [3-13]. The carried experiments indicate that C_{60} has high quantum yield in optic band, and it is possible to develop a device on the base of this photoresistive effect.

Using numeric calculations and experimental absorption spectra of individual fullerenes it is possible to obtain optic response in IR- band for high or doped fullerenes. The interest in using the fullerenes in photoconductive sandwiches is explained by its band gap (E_g) comparable with E_g of widely used photosensitive semiconductive compounds such as CdTe (1.5eV) or CdSe (1.7eV). Therefore it is possible to create photodevice with high dark resistivity and low noise level. Technology of a thin film structure preparation is simple, reproducible and ecological.

The purpose of this work is to confirm the possibility of creating of IR- photosensitive fullerene sandwiches.

On the base of analysis of experimental results and theoretic researches the phenomenological model of charge carrier generation sub action of irradiation was present and carrier transport in thin film photoadvices was discussed. Possibility of IR- sensible advices realization on base of high fullerenes or doped fullerenes was present. It has been proposed to study Shottky transition and heterojunction with polymers for realization of all photosensitive properties of fullerenes. On the base of extended Huckel model numeric calculations of electron structure of high fullerenes and search of isomers with defined band gap value were made. Experimental researches of absorption spectra for UV-, optic and IR- bands were done.

I. C_{60} FILM PHOTODETECTOR PHENOMENOLOGY

The C_{60} molecule has the truncated-icosahedral form shown in Fig.1, with a point-group symmetry I_h that allows the degeneracies as high as five [14-18]. The 30 filled $p\pi$ orbitals hold 60 electrons, in a pattern closely resembling that of free particles on the surface of a sphere (Fig.2) [19]. The highest-occupied orbital of neutral C_{60} is the completely filled five-fold degenerate h_u orbital, and the lowest unoccupied orbital, which is central to anionic compounds, is the threefold degenerate t_{1u} orbital some 2-3 eV higher in energy [20].

Fullerite is a molecular solid held together primarily by weak dispersion interaction, with a cohesive energy of only 1.4 eV/molecule (with respect to C_{60} vapor [21]). The molecular structure and the internal electronic and vibration excitation energies, at ambient pressure, are hardly different from those of the isolated molecule. The solid is highly compressible, whereas the molecular structure is essentially incompressible. [22] Electronically and optically, it may be regarded as a large bandgap semiconductor, with a gap near to 1.7 eV, as only a small dispersion into bands of E 0.5 eV full width is indicated. [23].

The crystalline state of solid places the molecular centers at the lattice points of a face-centered cubic lattice (fcc). [24]. The fcc lattice constant is $a=14.15$ Å, the van der Waals diameter of the molecule is 10.01 Å. As in most crystals composed of high symmetry molecules, the modes associated with molecular orientation are very soft and active, leading in C_{60} fullerite to orientational ordering transitions from a high temperature rotator phase to a partially oriented phase at (225K), and then near 90K to oriented phase, with residual static orientational disorder having well-defined librational excitations (librons). [25,26].

The electronic and optical properties of C_{60} in the fcc lattice have been studied by a first-principles method. [27]. It is shown that C_{60} has a low dielectric constant and an optical spectrum rich in structures. The spectrum shows five disconnec-

ted absorption bands in the 1.4 to 7.0 eV region with sharp structures in each band that can be attributed to critical-point transitions. This is a manifestation of the localized molecular structure connected with long range crystalline order.

Figure 3 shows the calculated band structure near the gap. There are direct band gaps of 1.34 eV at X and 1.87 eV at Γ . Since the local-density theory generally underestimates the band gap of an insulator, it is assumed that the true gap may be somewhat larger. The bandwidths of the top VB and the first set of unoccupied conduction bands (CB) are 0.55 and 0.54 eV, respectively. The averaged electron and hole effective masses at X are estimated to be 1.45 m and 1.17 m , respectively.

The enlarged $\epsilon_2(\omega)$ curve for this region is shown in Fig. 4. Transitions in a region near to 2 eV, from the top set of VB near the gap to the first set of unoccupied CB, are given in Fig. 3. The $\epsilon_2(\omega)$ curve shows the transition threshold to be at 1.46 eV, larger than the minimum direct gap of 1.34 eV at X. This is because the transition from the top of VB to the bottom of CB at X is symmetry forbidden. The transition threshold E appears to be from the top of VB to the second CB at X. One might expect that some transitions at other K points away from X would be allowed, such that the threshold may be at an energy between E_g and E_o . This was not the case because the dipole matrix elements for transitions in the vicinity of X are all vanishingly small. The small band gap leads to the speculation that an exciton may be formed at X in fcc C_{60} . The other structures in Fig. 4 can also be assigned to specific critical-point transitions. These critical-point transitions and the threshold are marked by arrows in the band diagram of Fig. 3.

The sharpness of optical transitions in fcc C_{60} is the result of the unique combination of a molecular cluster structure in C_{60} , which gives rise to the localized bands and the long-range fcc lattice. This gives the critical points in the Brillouin zone.

These theoretical results are confirmed by a number of further theoretical and experimental investigations [28-32].

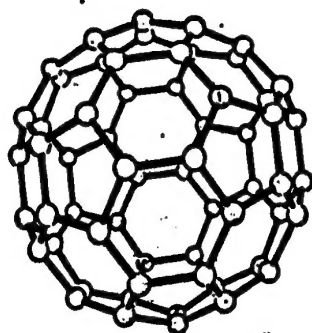


Fig.1 The structure of fullerenes C₆₀

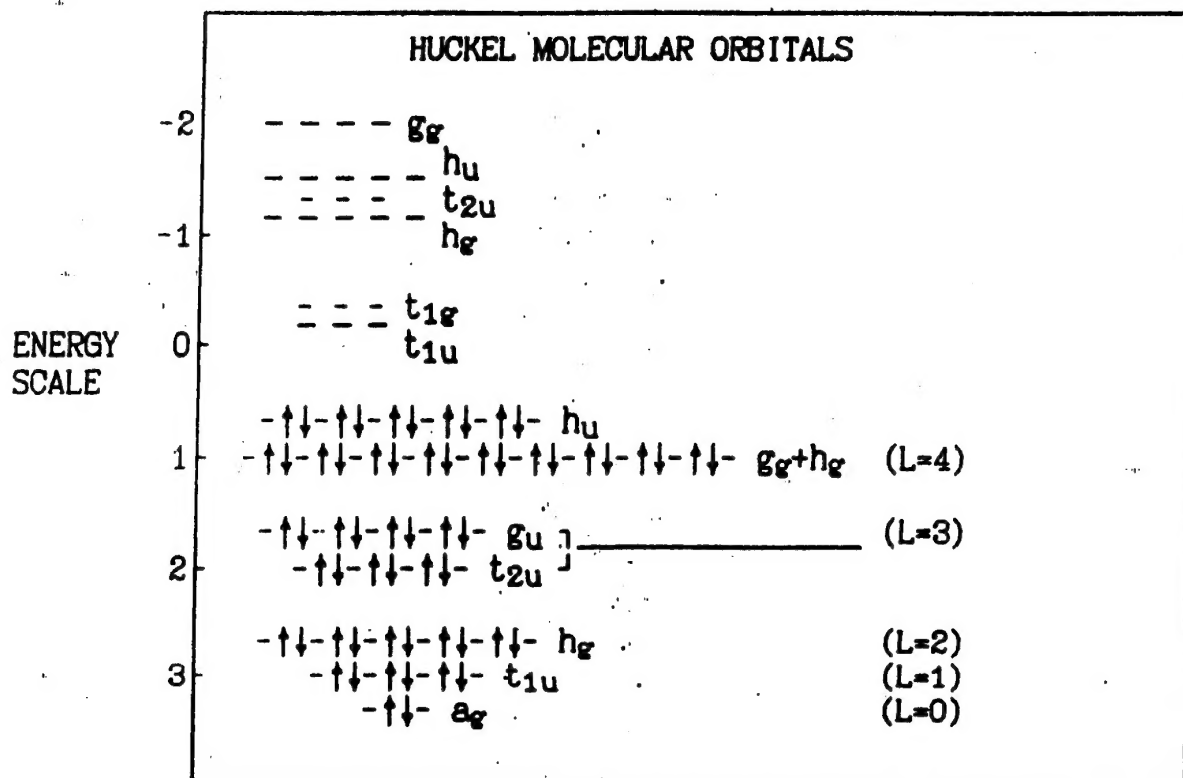


Fig 2 . Illustration of the π orbital levels in C₆₀

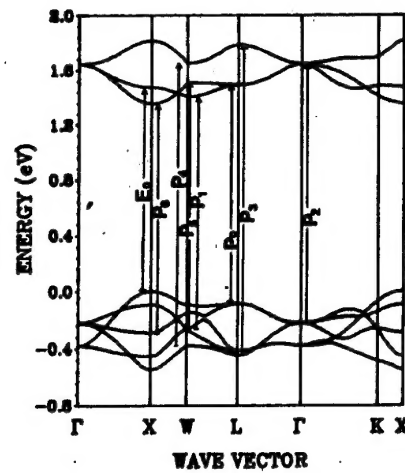


Fig.3 Calculated band structure of C60 in the fcc lattice near the gap. Arrows show critical-point transitions.

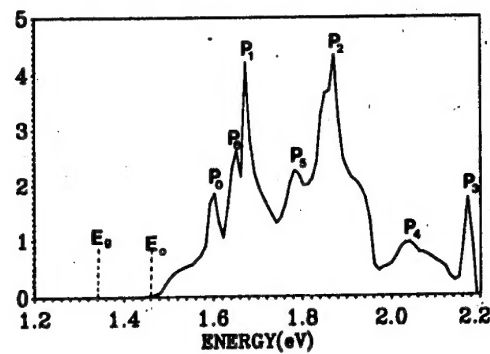


Fig.4 Imaginary part of the dielectric function of fcc C60 near the threshold. E_0 is the transition threshold. P_0 - P_6 are critical-point transitions marked in Fig.3

X. Wei et al. [33] have used various optical characterization techniques to study the electronic excited states in icosahedral clusters of C_{60} films produced by high-vacuum evaporation onto sapphire substrates. The experimental absorption spectrum $a(w)$ at 300K of a C_{60} film is shown in Fig. 5. There is a weak absorption band with a wide maximum at 2.9 eV. Molecular orbital calculations of the C_{60} molecule of icosahedral symmetry suggest that the irreducible representations of the HOMO and LUMO are h_u and t_{1u} , respectively. However, the full excited-state representations (taking into account all electrons) for the one-electron transition are T_{1g} , T_{2g} , G_g , and H_g . Optical transitions from the electronic ground state into these states are dipole forbidden; however, they become weakly allowed if one quantum of an ungerade vibrational normal mode is also involved in the transition process. From the various maxima in the visible absorption spectrum this may be a transition with phonon. The results obtained are confirmed by a number of papers [9-13, 28, 29].

So undoped C_{60} films are insulators and have significant visible absorption [34, 35]. J. Mort et al. investigated the photoconductivity in films of C_{60} [3, 4, 36]. The samples were deposited on glass slides, partially precoated with evaporated aluminum electrodes, by vacuum sublimation of C_{60} [14]. The sandwich cell geometry, in which the current flow is perpendicular to the plane of the film, minimizes the possible complications of more conductive surface layers which, if present, can dominate surface cell measurements.

The dark conductivity measurements made on these samples have demonstrated that the room temperature dark conductivity is $10^{-14} \text{ (}\Omega\text{m}\cdot\text{cm)}^{-1}$, and the dark current versus voltage curves are linear for applied voltage $< 2\text{V}$ [36]. Figure 7 shows a normalized spectral response curve at room temperature for photocurrents in a nominally undoped C_{60} film with an aluminum top electrode. The estimated peak photoefficiency is roughly 10^{-4} , provided that the current flow is limited by a carrier photo-generation rate.

Although this efficiency is low, the background dark currents are so small that the increase in current on illumination at 650 nm is about a factor of 10^2 (Fig.8).

Figure 6 shows an energy level picture based on published information regarding the ionization potential of solid C_{60} [37], its band structure [38], and the known work functions of aluminum and gold. It was shown to be highly unlikely that the photoeffects can be due to photoinjection of electrons from the metal electrodes. Therefore, it is suggested that the photocurrents are bulkgenerated photoconductivity in the C_{60} film.

S.Kazaoui et al.[37] investigated the photoconductivity of C_{60} thin films at 260-800 nm (with constant photon intensity $10^{14} \text{ cm}^{-2}\text{sec}^{-1}$). It is important to say that in these structures electric field is perpendicular to the illumination direction in gap electrode configuration used there, contrary to the sandwich configuration.

Figure 9 shows the absorption spectrum of an experimentally obtained C_{60} film which was kept strictly in vacuum after the deposition. The photoconductivity spectrum might be more reliable at low temperature because dark conductivity is very low and the light/dark conductivity ratio is greater than 100. "In situ" photocurrent spectra are presented in Fig.9 for both thin and thick films. For thin films (thickness ca. 25 nm) in the range $\lambda=260-800$ nm the photoconductivity spectrum follows almost the optical absorption spectrum, whereas for thick film (thickness ca. 200nm) above $\lambda=500\text{nm}$ an antibatic relation between the photoconductivity and the optical absorption spectrum is observed. Symbatic and antibatic relations between a photoconductivity spectrum and an absorption spectrum might be explained by bimolecular recombination.

Conductivity and photoconductivity temperature dependence give interesting insight to the photogeneration and carriers transport processes. Figure 11 show the temperature dependence of the dark current and photocurrent ($\lambda=300$ and 600nm) in the temperature range 170-380K. At low temperature regime $T<270\text{K}$, the conductivity and photoconductivity are weakly temperature

Optical
density
(a.u.)

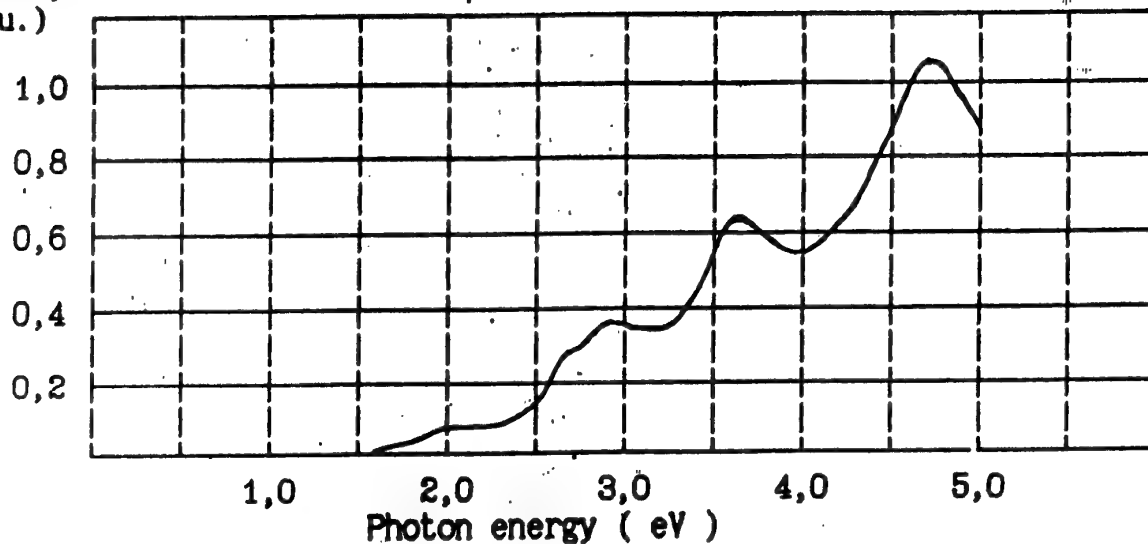


Fig.5 The optical absorption spectrum of a C60 film at room temperature.

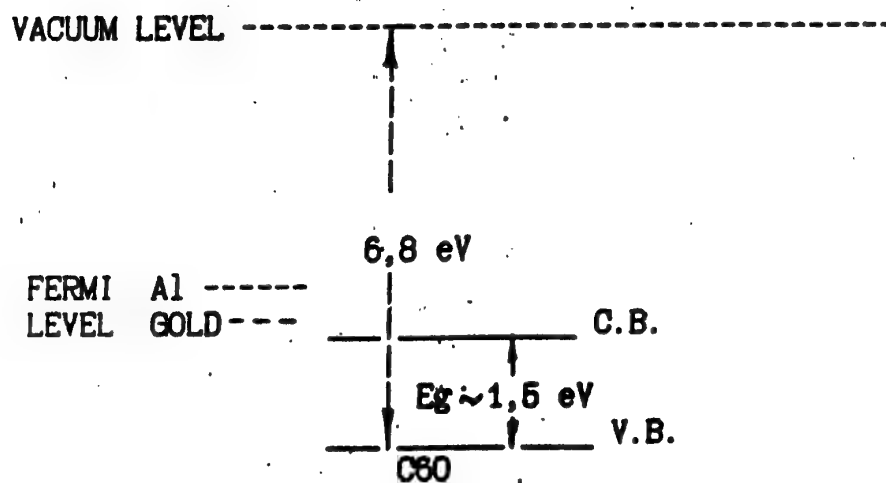


Fig.6 Schematic representation of the energy level for C60, Al and gold relative to the vacuum level

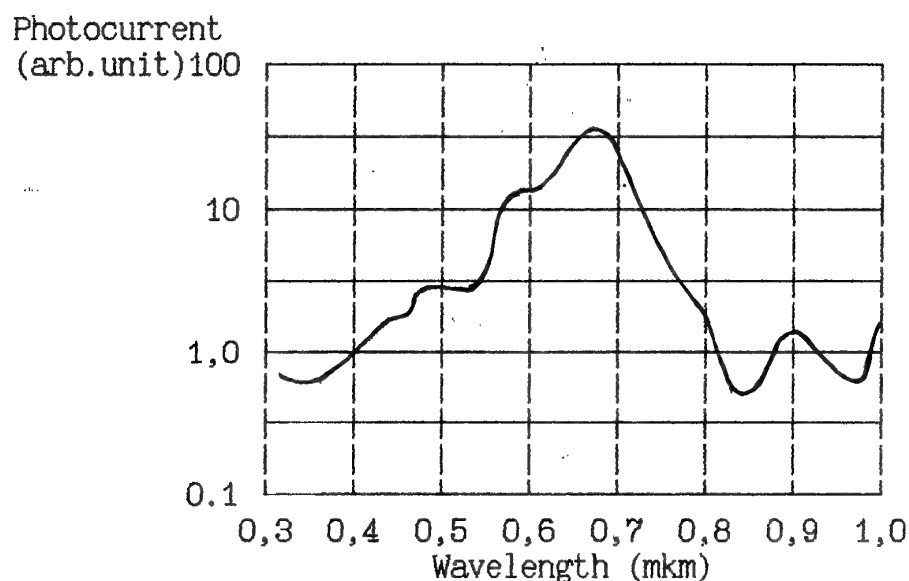


Fig. 7 Spectral dependence of the room temperature photocurrent in a C60 thin film. The photocurrent, in arbitrary units, is normalized for intensity.

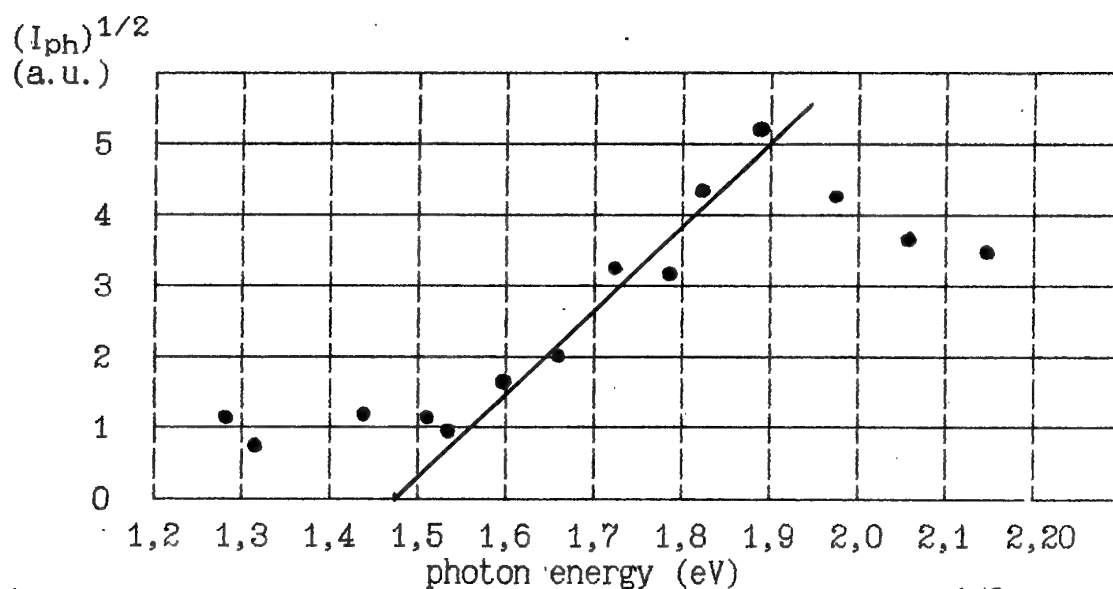


Fig. 8 Fowler-type, $(\text{photocurrent/incident photon})^{1/2}$ versus photon energy of the same data but over a limited range of photon energies. The intercept on the abscissa of the extrapolated linear region defines the photothreshold

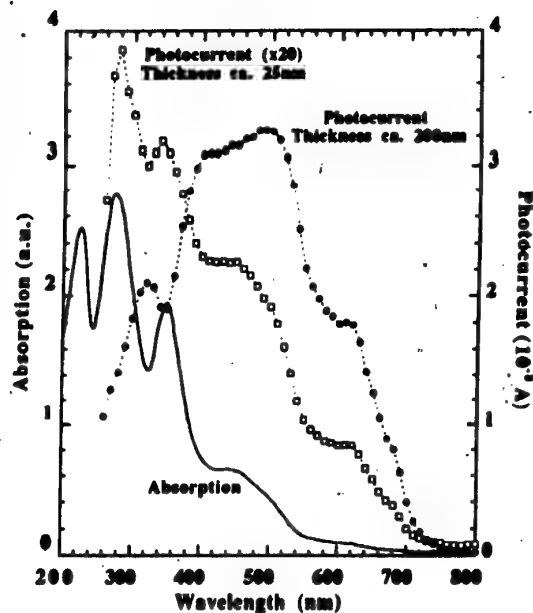


Fig.9 Absorption and photoconductivity spectra of C60 film.

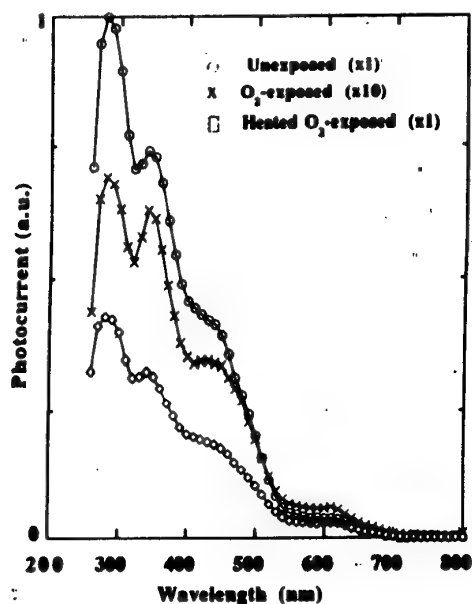


Fig.10 Photocurrent spectra at $T=260$ K, for unexposed, oxygen exposed and heated oxygen exposed films.

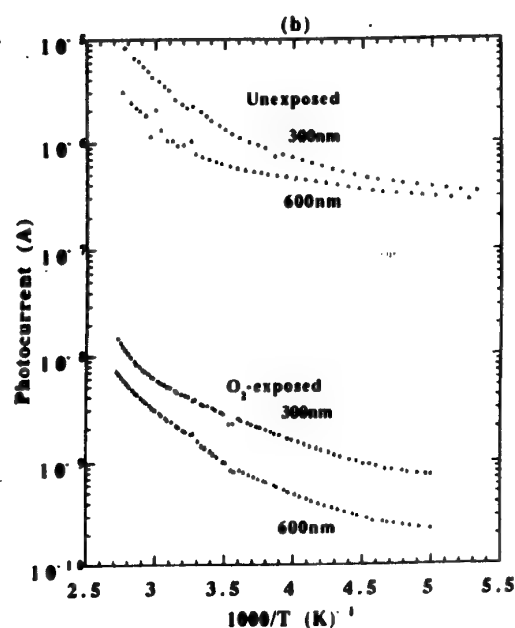
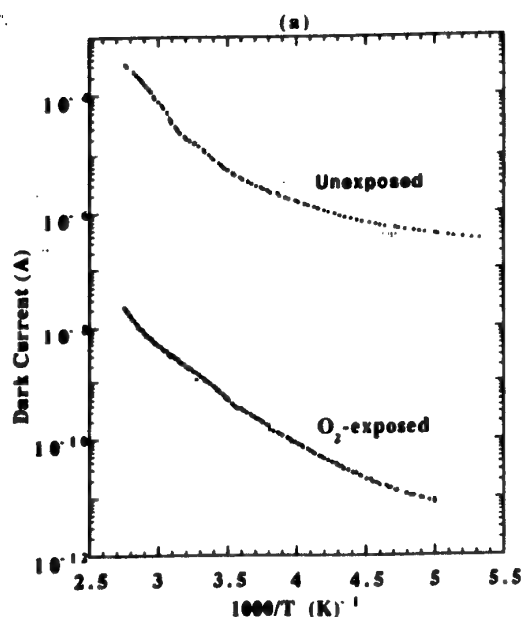


Fig.11 Temperature dependence: a) the dark current and b) photocurrent ($\lambda=300$ and 600 nm) "in situ" and oxygen exposed film

dependent. Moreover, here also the temperature dependence of the photoconductivity is similar for all excitation energy above 1.7 eV.

It is important to emphasize the effect of the atmosphere in which the C_{60} samples are exposed, and their electrical properties are measured. Preliminary experimental results, after a separate admission of pure nitrogen N_2 and pure oxygen O_2 , both with a pressure of 1 atm at room temperature, show that while N_2 causes no change, O_2 produces the principal effects in this material. The latter decreases σ_{ph} and σ_d by an order of magnitude; decreases the ratio σ_{ph} / σ_d ; decreases the photoconductivity response time; decreases σ_{ph} and σ_d which is even more important for a thicker film (200 nm) than a thinner film (13 nm). Figure 10 shows the temperature dependence of the dark current and photocurrent ($\lambda=300$ and 600 nm) for "in situ" and oxygen exposed in the temperature range 170-380 K.

As shown in Fig.11, neither the high nor the low temperature regimes are significantly affected by oxygen: the activation energy is constant. As far as the photoconductivity spectrum is concerned neither alteration nor new bands appear in unexposed and oxygen exposed samples (Fig.10).

Oxygen effect on the photoconductivity and conductivity as reflected by σ_{ph} and σ_d can be explained by assuming that oxygen is intercalated in the octahedral interstitial sites of the fcc lattice of C_{60} [11-13]. A common feature is that if the electrons, as major carriers, are easily captured and recombined in energetically deep traps at oxygen sites, then the carrier density, the free lifetime and drift mobility should decrease. Both the conductivity and photoconductivity might also decrease. In addition, intercalated oxygen does not alter or create new electronic states either in the subgap around 1eV, as reported by M.KAISER et al[13]. An alternative is that oxygen might act on the photogeneration process at the stage where the excited state should react with an electron donor with the formation of e/h pairs. On the other hand, the oxygen effect on photoconductivity has already been reported, but the

mechanism of it has not been finally established [10-13].

To interpret the carrier photogeneration and transport mechanisms, several candidates may be used, such as the Mott's law of variable range-hopping $\sigma(T) = \sigma_0 \exp\{-(T_0/T)^{1/4}\}$ or thermally activated process with weak activation energy at all excitation wavelengths.

Let us consider the photogeneration and charge transfer mechanism in a monocrystalline thin layer of a fullerene on condition of absence of any structural defects. In dealing with optical absorption, the most interesting for us are the low-energy transitions, such as electronic transitions from the ground state A_g to one of the three states, $1T_{1g}$, $1G_g$ and $1T_{2g}$. They are symmetry forbidden whereas the first allowed transition is assigned to $1T_{1u}$ ($h\nu = 3.5\text{eV}$ or $\approx 350\text{nm}$). In spite of the fact that absorption bands are the forbidden transitions for isolated molecules, they become weakly allowed in the solid as a result of lowering in symmetry due to intermolecular interactions.

The absorption coefficient is connected with falling photon energy (E_h) for symmetrically allowed falling transition as follows: $\alpha \sim (E_h - E_g)^{1/2}$ or $\alpha \sim (E_h - E_g)^{3/2}$ for symmetrically forbidden transitions [38]. The charge carrier photogeneration originates by means of transferring C_{60} molecules to an excited state with electron-hole pair formation and a further exciton ionization by external field or exciton-photon, exciton-exciton, exciton-dissociation centre interaction. The characteristic feature of the thin film structures with active layer thickness less than $1\mu\text{m}$ is large values of the electric field E , which are greater than 10^3 - 10^4 V/cm, for planar structures and more than 10^5 - 10^6 V/cm for the sandwich configuration. Since the value of electric field is more than the threshold value 10^3 V/cm (at which the exciton decay is observed), one can consider that generation and free carriers transfer occurs due to external field. In connection with weak p-orbital overlapping and carriers mobility less than $1\text{cm/V}\cdot\text{s}$ it is useful to consider the charge carriers moving basis on locali-

zed state model with photon-activated jumping mechanism. Since there is no exchange of energy in such electron jumps the charge transfer process occurs by means of two-stage scheme through the activated complexes. The transfer rate constant depends on electron overlapping of two neighbour molecules. The frequency of jumps is defined by perturbation theory: $\gamma_h = 2(\gamma - \alpha\beta)/h(1 - \alpha^2)$, where β, γ means the Coulomb and hopping integrals, respectively, and α is the orbitals crossing. Jump frequency defines the conductivity process in weakly interacting molecules with small orbitals overlapping, in which the vibrational relaxation time is approximately 10^{-13} s. The Coulomb term defines the interacting energy between charge densities with transitions on the single molecules, and in first approach $\beta \sim 1/r^3$.

The hopping interaction between orbitals decreases exponentially with the distance between molecules $\gamma \sim \exp(-Ar)$.

For the processes to be considered in the bcc structure with lattice constant $a_c = 14.15$ Å, both the jump's frequency and, consequently, the probability of the electron cross-jumping inside the activated complex defined by hopping interaction.

If ΔE_{ac} is the energy which is necessary to activate complex formation then the mobility is given by [39]:

$$\mu = (ea_c^2/kT) \gamma_h \exp(-\Delta E_{ac}/kT)$$

and the conductivity equation is:

$$\sigma = (e^2 a_c^2 / kT) \gamma_h N \exp(-(\Delta E_{ac} + \Delta E_{cc})/kT)$$

where ΔE_{cc} is the energy needed to free electron formation.

Value ΔE_{cc} is the result of several processes including the ionization stage and the carrier separation process. So the structure conductivity depends exponentially on excitation energy. It should be noted that energy E_{cc} may describe a succession of several processes (ionization, charge separation,

etc.). Every additional stage yields an exponential term. The given equation can be also used for the light conductivity dependence analysis, if the charge carrier recombination is taken into account by means of exponential term adding. In the absence of any dopant and crystal-lattice defects in fullerenes as well as in molecular crystals with low magnitude of the dielectric function the bimolecular recombination is apparently observed (the recombination between free carriers and opposite-charge ions).

The characteristic relations of the photoresistivity effect follow from the system of nonlinear differential continuity equations and the Poisson equations solution with the choice of the boundary conditions by taking into account the real structure's configuration [40]. The obtained analytical [41] and numerical [42] solutions of the continuity equation for the molecular crystals can be used in the photoreceiving structure (based on C_{2n}) analysis too.

Figure 12 is the explanation of the relaxation of excited states and photocarrier generation in C_{60} thin film based on the steady-state photoconductivity measurements. Due to the photon absorption (excitation wavelength is 300 or 600 nm), C_{60} transits from the electronic ground state to the excited state. The fact that the shape and the wavelength position of the main peak (maximum of the luminescence emission at 730nm) of the luminescence emission spectrum are irrespective of the excitation energy indicates that the internal conversion takes place to the lowest localized excited electronic states.

The temperature dependence of the photoconductivity shows that the activation energy is $E_a(6\text{ ph}) = 0.2\text{ eV}$ ($T > 270\text{K}$) for all excitation wavelengths ($\lambda = 300\text{-}600\text{nm}$). We should keep in mind that the temperature dependence of steady-state photoconductivity reflects that of Φ , and it may complicate the analysis. On the one hand, this result shows that excitation process generates e/h pairs which further require thermal and electric energies to create free carriers. On the other, the excited molecules decay to the same localized electronic states irres-

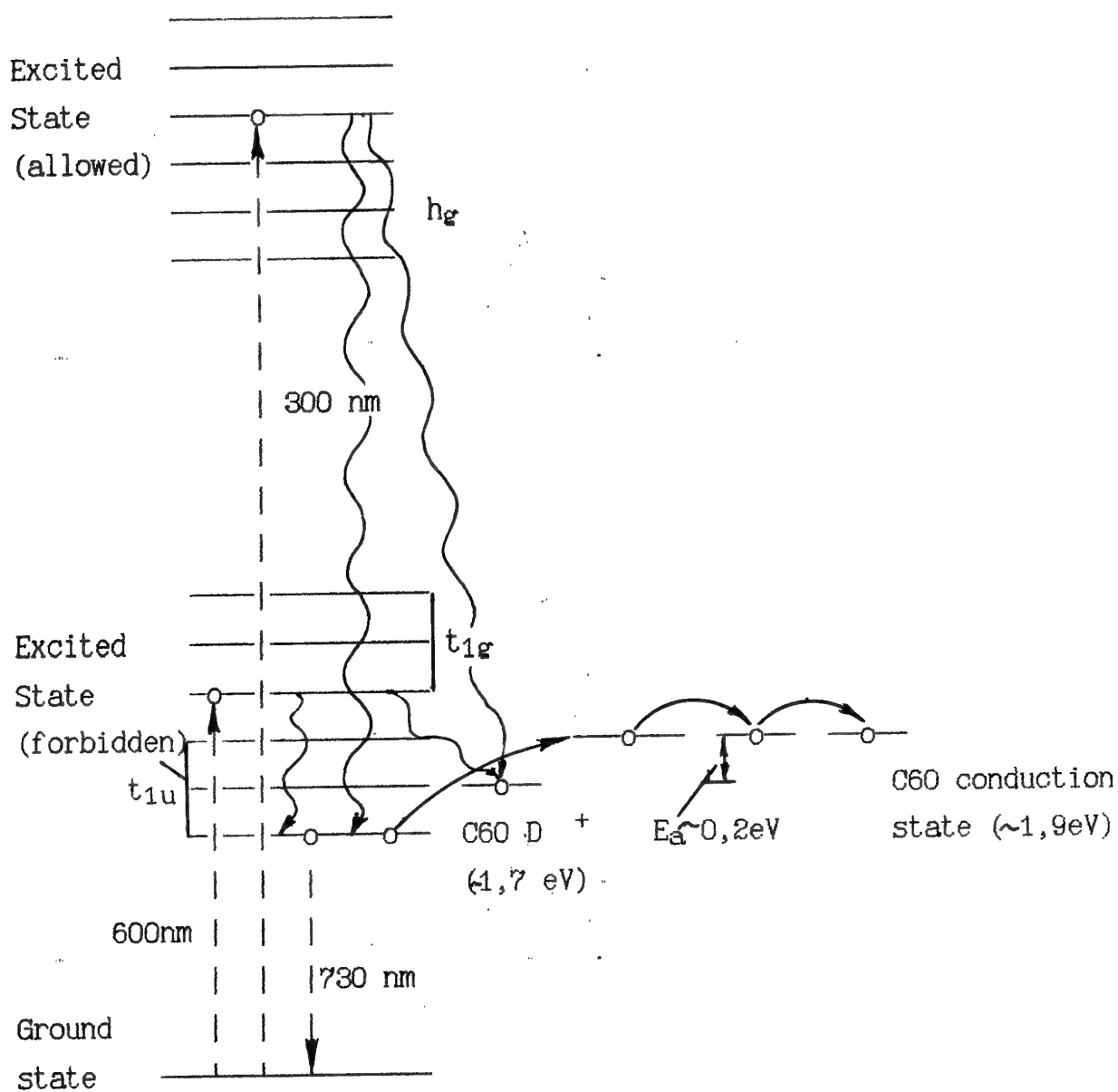


Figure 12 Schematic representation of the relaxation of excited states and photocarrier generation in C60 thin film.

pective of the excitation energy. This suggests that carrier photogeneration might occur from the lowest excited state of Frenkel-type exciton carrying a substantial charge transfer character.

The intrinsic conduction state has been estimated at 1.9 eV [43]. This result together with the measured energy activation $E_a(\delta_{ph}) = 0.2 \text{ eV}$ indicates that the precursor for photogeneration is 1.7 eV above the electronic ground state. This value approximately corresponds to the emission wavelength of 730 nm. Transport of the carriers might happen in narrow conduction states by hopping from site to site. Once electrons and holes have been freed they will remain free until they are captured by an imperfection, or recombine. As already mentioned, the bimolecular recombination process shortens the free carrier life time. Reported transient photoconductivity measurements on C_{60} thin film show that carrier recombination process takes place in the time scale of pico-second to several hundred pico-seconds (5). In the case of bimolecular recombination processes the steady-state photocurrent can be expressed by the following equation:

$$I_{ph} = (\Phi \eta / \alpha \gamma)^{1/2} e s \mu E (1 - \exp(-\alpha d / 2)) / d$$

($\eta, \gamma, \mu, s, \Phi$ are respectively quantum yield, bimolecular recombination coefficient, mobility, geometry factor, photon flux) [6]. Experimental evidence shows that photocurrent is proportional to Φ^n with $n=0.5$ at $T=300 \text{ K}$ and $n=0.8$ at $T=150 \text{ K}$ in the range $10^{13} - 10^{15} \text{ cm}^{-2} \text{ sec}^{-1}$. On illuminating the conductivity changes from $\delta_d = 7.5 \times 10^{-5}$ to $\delta_{ph} = 3.5 \times 10^{-6} (\text{Ohm} \cdot \text{cm})^{-1}$.

In the perfect structure the charge localization occurs owing to an interaction between the charge carriers and the crystal lattice. In practice, however, chemical impurities and structural defects have major influence on conductivity of molecular crystals.

The presence of the local structural defects results in the formation of traps for charge carriers and excited states. Crystal lattice is disturbed near a structural defect, which further changes the interaction energy between a lattice and

a charge carrier. So the charge will be localized near a structural defect.

The local lattice deformation results in change of both excited and ground states energy levels with respect to appropriate levels in volume (a space-shift term). The difference in ionization potentials between molecules in the crystal defines the levels of impurity depth, which is the charge carriers traps.

In dealing with processes in thin layers of fullerene one have to take into consideration the polycrystalline structure of the active layer. Such a structure leads to an appearance of the potential barriers at the corners' boundaries, which results in the spatial charge formation.

In the considered structure with Ohm's contacts the charge transfer process depends on a free carrier injection from the contacts. At low voltages applied to a carrier the injection will be small, the charge carriers concentration in the absence of voltage is larger than density of the carriers injected, and the current is in agreement with Ohm's law. If this condition is not executed, then the current is restricted by space charge. Into the volume of the material the additional charges are injected, the potential of which has an influence on volt-ampere function.

The presence of the structure defects and chemical impurities makes the consideration of the carriers generation carrier transfer mechanism quite complicated. One should take into consideration both the free charges and the excited states localization on traps as well as the delocalizations effects due to photon interaction. The problem to be solved becomes even more complicated owing to oxygen doping of the photoconductive material. Such doping leads to surface state evolution, potential barriers formation and origination of the space charge region. The oxygen influence changes the parameters of the photoreceiving structures (based on metal phthalocyanine (Me-PcM-Me) by more than a factor of 10. [44]

The lack of investigations results does not allow a full so-

lution of the problem of choosing the factors, which determine the photogeneration and charge transferring, in the structures with photosensitivity layer based on fullerenes. However, it is possible to name some general conditions of transferring the effect into IR band: decreasing of the gap due to upper fullerene or the doped fullerene having additional levels in the forbidden band.

It is well known that the crystalline state of the solid fullerene C_{60} places the molecular centers at the points of a face-centered cubic lattice (fcc). The close packing of these molecules leaves a regular array of cavities sufficient for small molecules or atoms such as, for example, alkali-metal atoms. The alkali ions occupy the octahedral and tetrahedral vacancies of the most C_{60} lattice. This makes the diffraction intensities drastically altered from those of C_{60} fullerite. The scattering centers in fullerite are located not on the fcc lattice points, but rather displaced radially to a distance, leading to dramatic near-cancellations for some lines; the presence of the alkali ions as strong scatterers drastically modifies this condition.

Reaction of solid C_{60} with alkali metal to form various alkali-fulleride compounds can be achieved as a vapor-solid reaction, or in a suitable liquid solution (solvent), or as a solid-solid reaction. It is important that after such doping (as now known) stoichiometric compounds would be strongly preferred in these mixtures, that allows one to predict some common properties of these materials.

Figure 2 shows a number of Huckel molecular orbitals of the pure C_{60} fullerene. (In solid C_{60} there are no such distinct levels. They have a width approximately 0.2-0.04 eV). The most simple model, which allows one to describe alkali-doped fullerene properties, becomes clear from this figure.

Really, since the t_{1u} (LUMO) band of C_{60} is of 3-degeneracy, for the solids MxC_{60} ($x=0-6$), the carrier concentrations in energy bands gradually increase when $x=0-1-2-3$, and so do their conductivities. Furthermore, for the solids M_xC_{60}

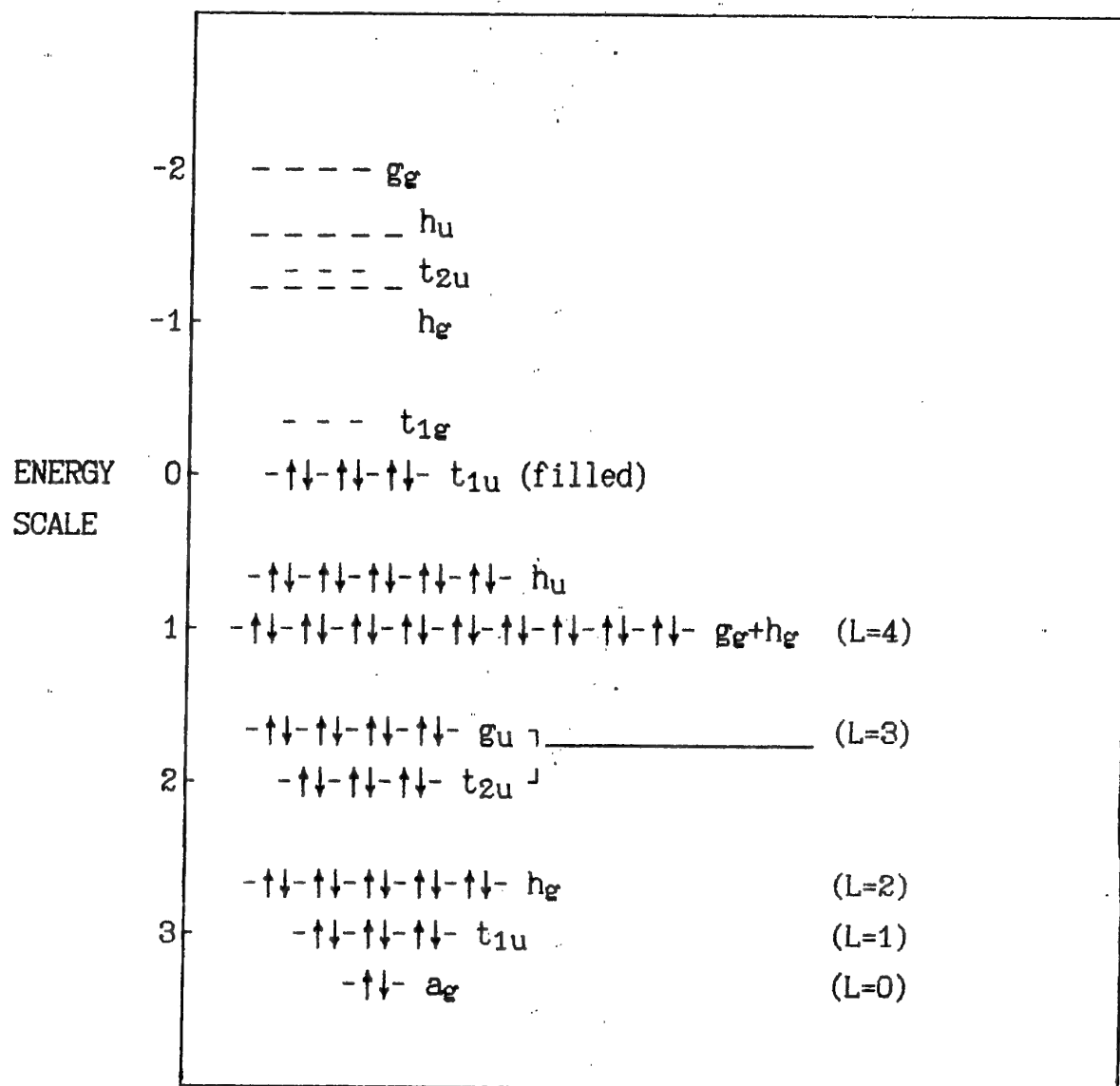


Fig 13. Illustration of the $p\pi$ orbital levels in Me_6C_{60} . The most longwave dipole allowed transition is $t_{1u} \rightarrow t_{1g}$.

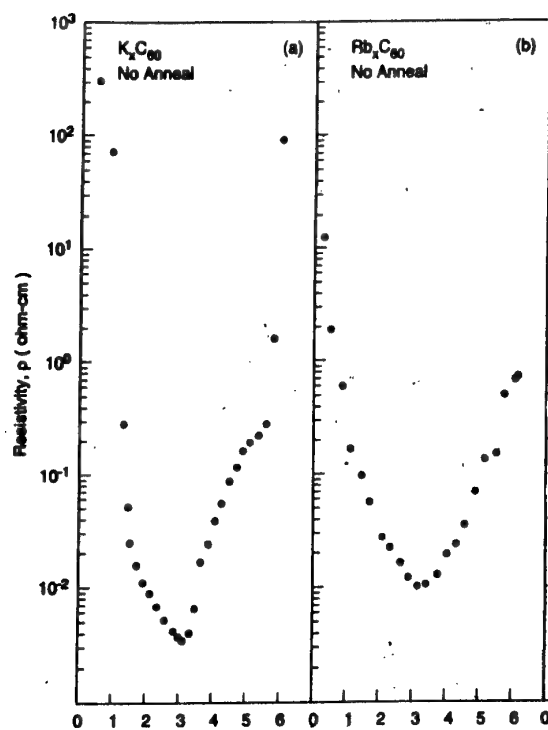


Fig.14 Resistivity of doped fullerene (Me_xC_{60}) films

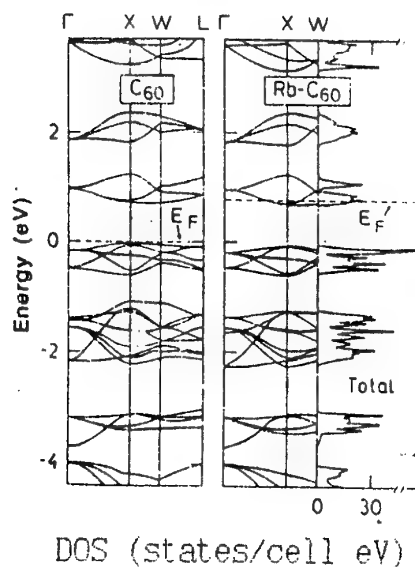
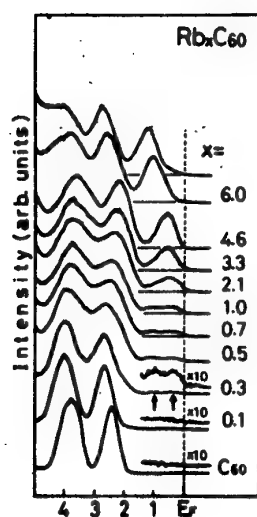


Fig.15 Photoemission spectra of Rb_xC_{60} measured at $h\nu=20\text{eV}$

Fig.16 LDA-LMTO band structures of C_{60} and RbC_{60} in the fcc structure.

($x=0-6$), the carrier concentrations in energy bands gradually decrease when $x=3-4-5-6$, and so do their conductivities.

The t_{1u} band is fully filled when $x=6$, and the M_xC_{60} is transformed to an insulator again (see Fig.13)

Such behavior is confirmed, in general, by the experimental measurements on conductivity of doped fullerenes (see Fig.14) [45]. The rigid band calculations also predict a large HOMO-LUMO gap and narrow bands at all doping concentrations. Furthermore, with increasing x the distance of the Fermi level from the HOMO band is expected to increase by an amount comparable to the narrow LUMO bandwidth. These would be the characteristic features of a rigid-band filling of the LUMO derived band upon doping and of negligible correlation effects [46]. (As an example, see Fig.16). This band structure calculation based essentially on a rigid-band model is obviously inconsistent with the experimental photoemission spectrum of doped C_{60} [47], which is shown in Fig.15. Upon a slight doping, the HOMO band (the highest occupied molecular orbital) originating from the five-fold degenerate h_u orbital C_{60} is shifted toward the high-binding-energy direction by about 0.3eV. This shift is due to occupation of gap states by electrons donated from Rb atoms. These gap states may arise from microscopic imperfection of a film and pin the Fermi level between the HOMO and the LUMO bands. Upon further doping, the HOMO band moves in reverse toward the Fermi level, and after approaching closest to the Fermi level moves away from it again. This peculiar shift of the HOMO band is not explained at all by a simple rigid-band model. The most remarkable change in the spectra is the appearance of a new band between the HOMO band and the Fermi level. At the early stage of doping the new band seems to consist of two subbands located at 0.3eV and 1eV, respectively, as indicated by arrows in Fig.16. However, the second subband at 1eV stops growing around the composition of $x=1$ while the first one continues to grow during the doping. Although both subbands are supposed to originate from the LUMO band of C_{60} , it is unknown at present why one of them stops growing while the other

one does not. In the change of the spectrum, we should remark that the photoemission spectrum has no sharp Fermi edge around the composition of $x=3$ where the LUMO band should be "half-filled", and as a result the maximum of the density of states should be at the Fermi level if a simple rigid-band model is applied.

Such unobvious electron spectra and conduction band evolution through doping may be explained by a number of reasons [47]:

- 1) Strong electronic correlation in LUMO band
- 2) Local lattice distortion caused by the doped electrons with produced polaron (or bipolaron) states. (In this case gradual growth of the additional band with the alkali doping may be described in terms of the increase of the density of polaron states).

However, in dealing with Me_6C_{60} compounds, these difficulties are not so important, because as will be seen below, the Me_6C_{60} electron structure should be of interest for the consideration of IR-band absorption.

In spite of the complicated structure of the conductive band in Me_xC_{60} , the numerical values of conductivity at $x=1, 2, 3, 4, 5$ allow one to make conclusion that the conductive band has, in general, the metal fashion, and therefore rather considerable free carrier concentration. So, using the compounds Me_xC_{60} with x (1,5) as a photoconductive material in photoresistance device is not perspective due to weak difference between dark and light currents and impossibility of the high electric field applied, which is necessary to quantum yield increasing.

Therefore the most appropriate materials for the photosensitive devices in the IR band will be the ones with fully filled t_{1u} band such as K_6C_{60} or Ba_3C_{60} . The magnitude of the static dielectric constant increases by a factor of about two upon doping: $\epsilon_1(0)=4.3$ in neutral C_{60} and $\epsilon_1(0)=7.1$ in Rb_6C_{60} . From consideration of the molecular orbitals structure of these compounds [48] (shown in Fig.13) it is obvious that there is a longwave transition between t_{1u} and t_{1g} bands with energy 0.4-0.6 eV or 2-3 μm . Moreover, this transition is dipole allo-

wed distinct from the most longwave transition h_g-t_{1u} in pure C_{60} , which is dipole forbidden.

In the experiments of Me_6C_{60} [49,50] the Frenkel exciton effects seem to be dominant, and the spectral shapes are not sensitive to the kind of dopants. Therefore, we can consider the photocarrier generation and charge transfer processes of the Me_6C_{60} by analogy with the previous C_{60} consideration.

So, the absorption in materials with fully filled t_{1u} band is shown to be significant in the IR band of spectrum. Using a doped upper fullerenes allows us to transfer the effect into far-IR band. Moreover, such strong doping causes the considerable deformation of the symmetrical structure of pure C_{60} crystal, resulting in additional increasing of the energy bands width and, therefore, the photoconductivity onset ($t_{1u}-t_{1g}$ energy value) is shifted toward the IR band.

In order to realize fully the photosensitivity properties of a fullerenes one should develop the structure based on rectifying contacts, and a first step in this direction will be a creation of the Schottky's contacts structures.

Figure 17 shows the Schottky's junction formation between a fullerene of electron conductivity type with work function Φ_s and a metal with work function Φ_m . At forming of the contact a region of a spatial charge appears due to electron transferring from fullerene into metal. The value of the energy barrier E_{sm} for an electron passing from fullerene into metal is given by: $E_{sm} = \Phi_m - \Phi_s$. And for the reverse process (from metal into fullerene) it is: $E_{ms} = \Phi_m - \Phi_s$.

On reverse bias applying, under action of external voltage V , the barrier height E_{ms} has remained the same, while the height E_{sm} has decreased. Current from fullerene into metal will be given by:

$$I_1 = I_s \exp(eV/kT)$$

where I_s means the saturation current.

The volt-ampere function is defined by Schokley's equation:

$$I = I_s (\exp(eV/kT) - 1)$$

where I means summary current.

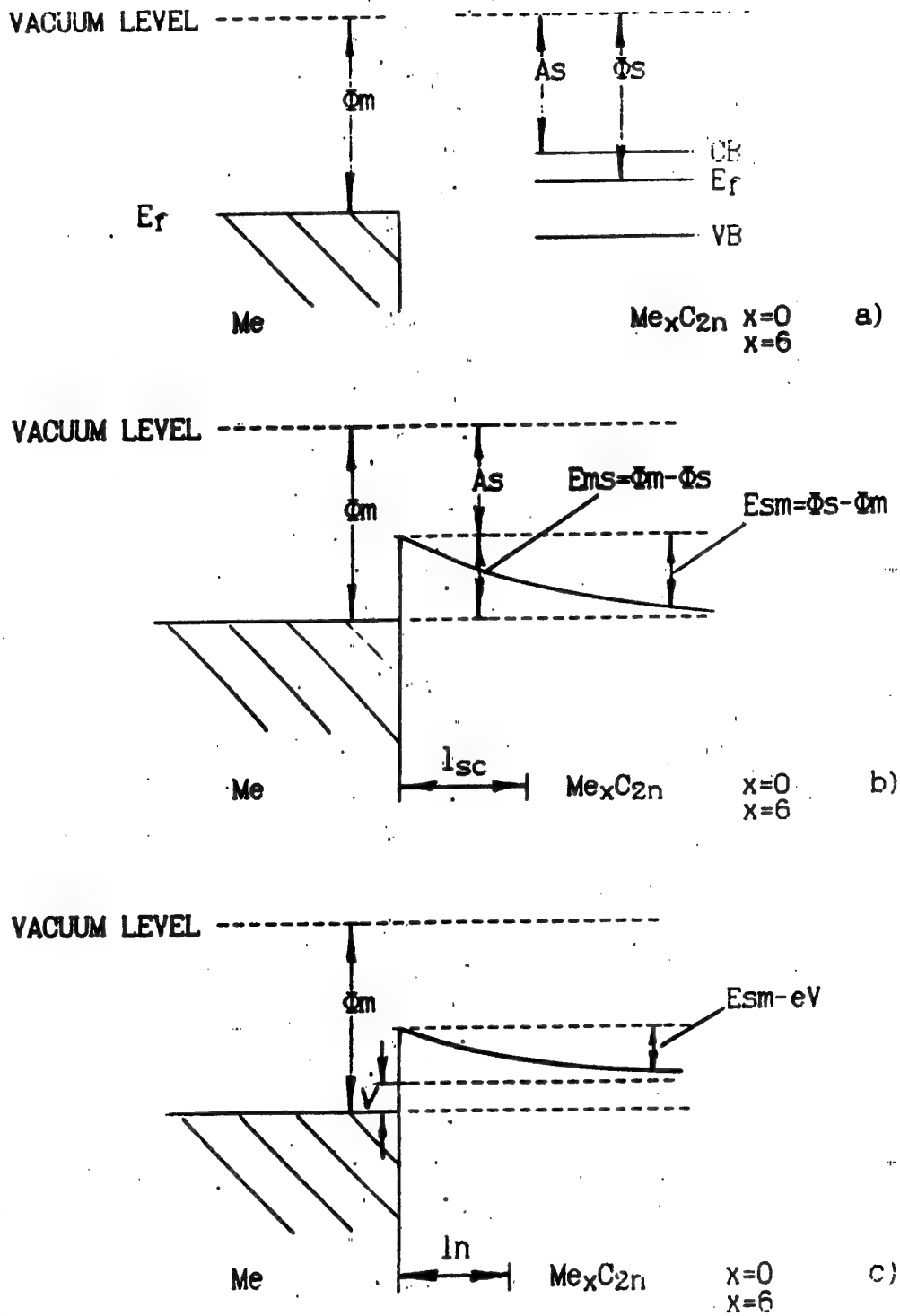


Fig.17 Schematic representation of rectifying junction
a) before contact formation
b) after contact formation
c) with reverse bias applied

In Schottkey's junctions the charge transfer process is determined by basic charge carriers of saturation current I_s :

$$I_s = A \exp(-E_{ms}/kT)$$

where A is a constant coefficient. On illuminating the sandwich configured structure the charge carriers photogeneration occurs owing to fullerene molecules transitions to an excited states and free carriers formation under the action of contact,

or the external difference of potentials.

The radiation may be absorbed in a metal, and it excites the electrons, which will go through the energy barrier E_{ms} . When the structure works as a photovoltaic cell the external applied voltage V makes the photocurrent I_{ps} somewhat higher due to electric field increasing and the recombination loss decreasing.

For thin fullerene films (100-500nm) the photogeneration will occur in the region of spatial charge. In comparison to the photoresistive effect the recombinative losses are considerably smaller.

Volt-Ampere function of the structure is described by the following equation:

$$(V - E_{sm})/R_h = I_{ph} - I_s (\exp(eV/kT) - 1) \\ I_{ph} = e\eta\alpha\Phi_0 (1 - \beta)$$

where means the quantum yield, Φ_0 , radiative flux, and β is the recombinative coefficient.

Schottkey's junction may also works in photogalvanic regime. In this case the excited state dissociation of the molecules occurs by means of contact potential difference influence only.

In the structure the free charge carriers transferring takes place under action of the contact field. The energy transferring also occurs due to probability exciton motion.

By analogy with molecular crystals the appeared potential difference V_x is proportional to the following terms:

$$V_x \sim kT/e \ln(I_{ph}/I_s + 1)$$

Obtaining the effect in IR - band for a Schottkey's junction will also be defined by narrow-gap or doped fullerenes application. For example, in order to obtain an optical response in 2-3 μm band with the application of doped fullerene K_6C_{60} it is possible to realize a Schottkey's junction by means of Ni or Pt ($\Phi_m=5.7\text{eV}$). An Ohm's contact can be manufactured with utilization of Al. To reduce the recombination losses one should make the width of a sensitive layer within the region of 25-100 nm.

It is known that after adding even a few amount of C_{60} into a semiconducting polymer the photosensitivity of material will be increased considerably [51]. The quantum yield will be increased too. This phenomenon is connected with the fact that C_{60} is an excellent electron acceptor capable of taking on as many as six electrons. Therefore, C_{60} forms charge transfer complexes with a variety of strong donors. In connection with the photoconducting phenomena the compositions of semiconducting polymers with undegenerate ground state or molecular crystals and fullerenes are the most interesting. In this case the optical absorption spectrum of the composition obtained is a simple superposition of the two components without any indication of states below gap of the semiconducting polymer due to interaction between these two materials in the ground state. The situation changes if we consider the photoluminescence spectrum of the material: in comparison with the semiconducting polymer alone one can see considerable quenching of the photoluminescence (by a factor of several orders), which proves strongly the domination of the photoexcited polymer - fullerene charge transfer process over the other possible processes (soliton formation, radiative and non-radiative recombination etc.) The rapid reducing of photoluminescence decay time confirms it too. Thus the quantum efficiency for the photoinduced charge transfer process is closed to unity.

To describe the transfer of the photoinducing charge from semiconducting polymer (donor) into the fullerene (acceptor)

one can use the known scheme, which consist of five steps (the dividing of this process into several steps is, of course, somewhat empirical, but permits one to describe sufficiently clearly the considered phenomena) [51].

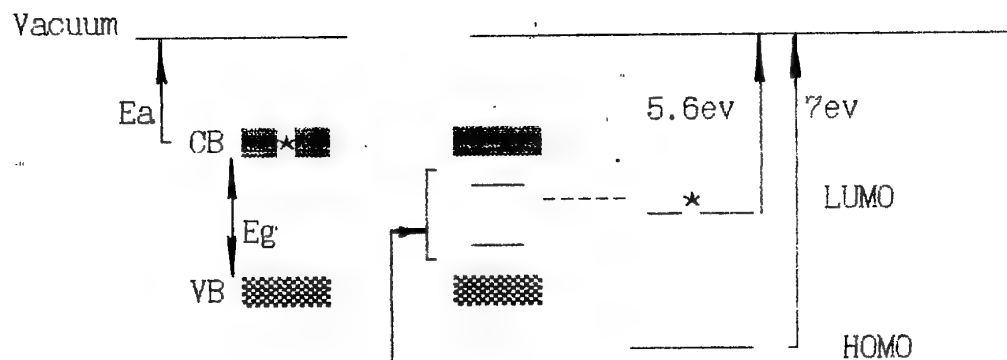
1. $D + A \rightarrow D^* + A$ (excitation donor)
2. $D^* + A \rightarrow (D - A)^*$ (excitation becomes delocalized on D-A complex)
3. $(D - A)^* \rightarrow (D^{a+} - A^{a-})^*$ (charge transfer initiated)
4. $(D^{a+} - A^{a-})^* \rightarrow (D^{+*} - A^{-*})$ (ion radical pair formed)
5. $(D^{+*} - A^{-*}) \rightarrow D^{+*} + A^{-*}$ (charge separation)

where D is the donor (polymer) and A is the acceptor (fullerene). Symbol * means the exciting state, 'a' is the number of charge transferred in units of electron's charge. The partial charge transfer at the third step is strongly dependent on the effects of the surrounding medium, such as the influence of the neighbor molecules, presence of external fields, etc. resulting in a continuous range for the transfer rate $0 < a < 1$.

At step 4, if $a=1$, a whole electron is transferred. At each step the D-A system can relax back to the ground state by means of several ways (releasing energy to the lattice, light emission, soliton formation). Step 4 does not occur when the ionization potential of the excited state of the donor is less than the sum of the electron affinity energy of the acceptor and the Coulomb energy of the separated radicals (including polarization effects).

The basic condition of the structure working according to that scheme is the prevailing of the charge separate process over the other possible schemes of the photoexcited state evolution. For this, it is necessary, in the first place, that the ground state of the semiconducting polymer should not be degenerate. If this is not the case the soliton formation process will be faster than the photoinduced charge transfer, so the structure will be weakly sensitive to light.

Longwave region of the spectrum will be first of all defined by the value of the polymer's energy gap, as well as the value of its electron affinity energy. It is convenient to consider



singlet polaron - exciton formation

E_a - is the electron affinity
 E_g - the value of the gap

. Fig.18 Schematic energy band diagram for the photoinduced electron transfer from semiconducting polymers onto C_{60}

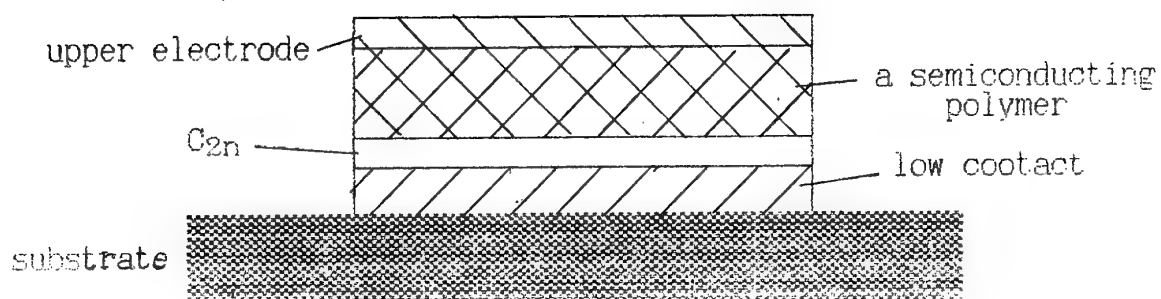


Fig.19 Schematic cross-section of the simplest possible heterojunction device.

the charge transfer process using the energy band scheme (Fig.18).

Upon illumination, an electron of the semiconducting polymer (donor) is excited across the energy gap (VB-CB). Due to very rapid structural relaxation into polarons, the two polaron states in the gap are created. This singled polaron-exciton experiences a rapid transfer (less than 10 s) transfer onto C_{60} by creating the polaron cations on the semiconducting polymer backbone and C_{60} anions. The back-relaxation process is dominated by phonon-assisted nonradiative recombination, which weakly influences the photoconductivity due to very fast electron transferring.

The negligible time of the photoinduced electron transfer has important consequences for photoconductivity, which are displayed by the experimental fact that the addition of C_{60} into the semiconducting polymer sensitizes the photoconductivity by means of enhancing the quantum efficiency for photo-generation of charge carriers and by inhibiting their recombination. Upon addition into a polymer of even 1% fullerene, the photocurrent increased by the factor of hundred[51], and one could observe a small shift of sensitivity into a longwave region of the spectrum (in comparison with photoconductivity of separate components).

The band scheme analysis permits us to make a conclusion that for transferring of considered effect into IR region one has to decrease, in appropriate way, the value of the polymer energy gap and that of the fullerene. However, it is necessary to remember about general essential condition between the ionization potential of the excited state of the polymer and the electron affinity of the fullerene as mentioned above. Seeking the appropriate polymer, it is also necessary, that its ground state should be undegenerate. According to our point of view the effect desired might be obtained by using the classes of bimetal ftolacians and upper fullerenes.

The most perspective structure, in this respect, is that with a heterojunction, the simplest of which is shown in Fig.19.

Really, by considering the band diagram, one can immediately see that a heterojunction formed at the interface between semiconducting polymer and fullerene thin films should exhibit a rectifying current-voltage characteristic (analogous to p-n junctions). One polarity of such device (with electron injection on the semiconducting polymer side and electron removal on fullerene) is energetically unfavorable, and it therefore results in very low current densities. On the other hand, the electron injection on to fullerene and electron removal from polymer are energetically favorable, which creates the conducting species on both sides. This polarity of the device results in relatively high current densities. So the rectification ratio reaches several orders in magnitude. As expected from the observation of fast photoinduced electron transfer from polymer to fullerene, a major increase in both forward and reverse bias current is observed to result from photoinduced charge separation at the heterojunction interface, upon illumination.

The longwave threshold of sensitivity of such structure will be defined both by the value of polymer energy gap [52,53] and by the fullerene's one (intrinsic photoeffect in fullerene). For the IR region 3-5 μm the polymer's gap must be about 0.2-0.3 eV, and its electron affinity must be approximately 5.5 eV.

In the visible area of spectrum the electron photogeneration occurs in two ways: charge transfer (from polymer to fullerene) process and photoionization process of the fullerene itself; in the IR band of spectrum (especially if C_{60} is used the first process is fully dominated. It is necessary, however, to take into account that the diffusion of charge carriers in such devices is limited, i.e. the photoactive region is restricted to a thin layer adjacent to the interface between the polymer and fullerene layers.

Therefore, the semiconducting polymer layer acts as a filter, which reduces the number of photons reaching the photoactive interface, and, consequently, reduces the photosensitivity of the structure. Maximum of such absorption will be at the re-

gion of spectrum, appropriate to the value of polymer's energy gap, i.e. just in the IR region which is of interest. Therefore, it is necessary to choose the polymer so that its absorption peak was within the region of 3-5 μm .

So the photoconducting devices on the base of heterojunction between the semiconducting polymer or molecular crystals and the fullerene are shown to be perspective for the photoreceiving IR devices.

REFERENCES TO CHAPTER I

1. N. Minami, Chem. Lett., 1991, 1791 (1991).
2. K. Pichler et al., J. Phys.: Condens. Matter, 3, 9259 (1991).
3. J. Mort et al., Philos. Mag. Lett., 67, 77 (1993).
4. J. Mort et al., Appl. Phys. Lett., 61, 1829 (1992).
5. C. H. Lee et al., Phys. Rev. B, 48, 8506 (1993).
6. G. Giro et al., Chem. Phys. Lett., 211, 580 (1993).
7. M. Kaiser et al., Synth. Met., 51, 251 (1992).
8. H. Yonehara and C. Pac, Appl. Phys. Lett., 61, 575 (1992).
9. T. Arai et al., Solid State Commun., 84, 827 (1992).
10. N. Minami and M. Sato, Synth. Met., 55-57, 3092 (1993).
11. A. Hamed et al., Phys. Rev. B, 47, 10873 (1993).
12. A. Zahad and L. Firlej, Solid State Commun., 87, 893 (1993).
13. M. Kaiser et al., Solid State Commun., 87, 281 (1993).
14. W. Kratschmer, L. D. Lamb, K. Fostiropoulos, and D. R. Huffman, Nature 347, 354-358 (1990).
15. H. W. Kroto et al., Nature 318, 162 (1985).
16. Mat. Res. Soc. Symp. Proc., 206 (1991).
17. Acc. Chem. Res. 25 (1991).
18. F. Diederich and R. L. Whetten, Acc. Chem. Res., 25, 121 (1991).
19. R. C. Haddon et al., Chem. Phys. Lett., 125, 459 (1986), 165 (1986).
20. C. Reber et al., J. Phys. Chem., 95, 2127 (1991).
21. A. Tokmakoff et al., Chem. Phys. Lett., 186, 450 (1991).
22. S. Duclos et al., Nature, 351, 380 (1991).
23. C. T. Chen et al., Nature 352, 603. (1991).
24. R. Fleming et al., Mat. Res. Soc. Symp. proc., 206 (1991).

25. W. I. F. David et al., Nature, 353, 147 (1991).
26. D. A. Neumann et al., J. Chem. Phys. (submitted). W. P. Beyerman et al., Phys. Rev. Lett., 68, 2046 (1992).
27. W. Y. Ching et al., Phys. Rev. Lett., vol. 67, N 15 (1991).
28. J. S. Merth, H. Vanherzeele and Y. Wang, Chem. Phys. Lett., 197, 26, (1992).
29. Z. H. Kafafi, J. R. Lindle et al., Chem. Phys. Lett., 188, 492 (1992).
30. K. Harigaya and S. Abe, Jpn. J. Appl. Phys., 31, L887 (1992).
31. K. Harigaya and S. Abe, J. Lumin., 60, 380 (1994).
32. K. Harigaya and S. Abe, Phys. Rev. B, 49, 16746 (1994).
33. X. Wei et al. Synt. Metals, 49-50, 549-555, N 1-2 (1992).
34. R. C. Haddon et al. Nature, 350, 320 (1991).
35. A. F. Hebart, M. J. Rosseinsky, R. C. Haddon, D. W. Murphy, S. H. Glarum, T. T. M. Palstra, A. P. Ramirez and A. R. Kortan, Nature, 350, 600 (1991).
36. J. Mort, R. Ziolo, M. Machokin, D. R. Huffman and M. I. Ferguson, Chem. Phys. Letters, 186, 284 (1991).
37. S. Kazaoui et al., Solid State Commun., Vol. 90, 10, pp. 623-628 (1994).
38. S. Nudelman et al., Optical Properties of Solids, New York, (1969).
39. H. Meier, Organic Semiconductors, Berlin, 1974.
40. J. S. Bonham et al., Aust. J. Chem., 30, 705 (1977).
41. N. Sinharay et al., Sol. St. Electron, 7, 125 (1964).
42. T. J. O'Reilly et al., Sol. St. Electron, 18, 965 (1975).
43. R. K. Kremer et al., Appl. Phys. A, 56, 221 (1993).
44. M. Martin et al., J. Appl. Phys., 54, 2792 (1983).
45. R. C. Haddon et al., Chem. Phys. Lett., 218, 100-106 (1994).
46. S. Satpathy et al., Phys. Rev. B, vol. 46, N3, 1773 (1992).
47. T. Takahashi., Com. Cond. Mat. Phys. vol. 16, N2, 113-123 (1992).
48. K. Harigaya., J. Appl. Phys., vol. 33, 1093-1095 (1994).
49. T. Pichler et al., Sol. St. Commun., 81, 859 (1992).
50. W. L. Wilson et al., Phys. Rev. B, 48, 2738 (1993).
51. N. S. Sariciftci et al., Int. J. of Modern Phys. B, vol. 8, N3 (1994).
52. H. Eckhart et al., J. Chem. Phys., 91, 1303 (1989).

53.S.Yamada et al., J.Chem.Soc.Chem. Commun. 1448 (1987)

II. HUCKEL TREATMENT OF HIGH FULLERENES FOR THE CALCULATION OF BAND GAP

Recently the fullerene family C_n with a hollow cage structure has been intensively investigated. Various optical experiments have been performed, and interesting properties due to π -electrons delocalization on molecular surfaces have been revealed. They include the optical absorption spectra of C_{60} and C_{70} [1,2], and the large optical nonlinearity of C_{60} [3,4]. The absorption spectra of higher fullerenes have also been obtained [5,6]. In order to analyze the optical properties of C_{76} , K.Harigava studied the linear absorption using a tight binding model [7], and a model with a long-range Coulomb interaction [8] and the Hartree-Fock approximation with the parameters, which reproduce the main feature of C_{60} and C_{70} . Figures 20 and 21 show the experimental spectra C_{60} and C_{70} and the calculated spectra [9] for optimized parameters. Experimental data are taken from refs.1 and 2 and are shown by thin lines.

There are three main features in C_{60} absorption spectrum over the energies 3.5eV, 4.7eV and 5.6eV. In the case of C_{70} we could say that several small peaks in the energy interval from 1.7eV to 3.6eV have been originated from a 3.5eV feature of C_{60} after the splitting. The 4.7eV and 5.6eV features of C_{60} transfer in a large feature over the energy region larger than 3.6 eV. The optical gap decreases from 3.1eV (C_{60}) to 1.7eV (C_{70}). It is seen that relative intensities differ very much for the indicated fullerenes, but the band gap values have a little difference.

Figure 22 represents experimental data and results of calculations [9] for C_{76} . The main feature is the same - dislocati-

on of optical gap to lower values (0.7-1.2eV) for high fullerenes.

The Huckel treatment [10] of fullerenes with Ih symmetry made for C₆₀, C₂₄₀, C₅₄₀, C₉₆₀, C₁₅₀₀, C₂₁₆₀ and C₂₉₄₀ indicates that all these fullerenes must be stable, and the band gap is getting lower for higher fullerenes as seen from Table 1.

Table 1

Comparison of calculated results for fullerenes C(60i).

Cn	HOMO	LUMO	Gap
C ₆₀	0.6180	-0.1386	0.7566
C ₂₄₀	0.4368	-0.0597	0.4965
C ₅₄₀	0.3241	-0.0337	0.3578
C ₉₆₀	0.2550	-0.0222	0.2772
C ₁₅₀₀	0.2096	-0.0160	0.2256
C ₂₁₆₀	0.1777	-0.0122	0.1899
C ₂₉₄₀	0.1541	-0.0097	0.1637

Previous experiments showed also that the optical gap decreases in higher fullerenes, and thus this property is consistent with the recent calculations. However many small structures in the experimental absorption of C₇₆ [5] which is shown in Fig.22 are not so apparent. Therefore it is difficult to perform a detailed comparison with calculated results. The agreement between the calculated and experimental results is worse for higher fullerenes.

Therefore we try to calculate the band gap of high fullerenes only. Such calculations are very important in order to predict a possibility of optical absorption in the indicated spectral region (for example, 3000- 5000nm). For high size molecules, such as fullerenes Cn, with n greater than 100 the optimal method is the expanded Huckel method (EHM).

This method evaluates all valent electrons, using the superposition integrals of Slater-type s-, p- A0 for the preparation of a Hamiltonian and the experimental ionization potentials.

We used a standard geometry of systems with conjugate bonds.

The main object of this study is determination of fullerene type that has the band gap (DE) of 0.2eV or less.

1. Preparation of geometrical constructions of isomers C_n .

All geometrical constructions of C_n that we use have the following characteristics.

1. Fullerene molecule is a hollow polyhedric cage with conjugated bonds.

2. Fullerene molecule consists from 12 non-adjoining five-member rings, that are surrounded by six-atom rings.

3. Every molecular structure is modelled using two equal fragments C_m (where $m = 36, 40, 46, 50, 55$).

4. Two fragments are connected directly, or by using the additional carbon atoms. Type of the formed fullerene isomer depends on fragment symmetry and relative fragment positions.

We present flat diagrams of connection of fragments that form the studied fullerenes (Figs. 23-26).

5. On the base of flat diagrams the hollow closed cages with the preliminarily indicated bond length (difference not more than 0.002Å) were prepared.

Geometrical structures of the studied fullerenes are presented in Figs. 27-52.

2. Calculation of fullerene band gap

Firstly we tested different methods of calculation by C_{60} , C_{70} and C_{76} . We compared INDO, CNDO/2, and EHM. A comparison of the results indicated that INDO and CNDO/2 give energies higher than experimental. Only EHM gives values near to the experimental ones.

The results of calculations by EHM are presented in Table 2 and Fig. 53.

Note that the obtained energies for C_{80} are degenerate. This corresponds to molecular instability and agrees with the experimental data that such fullerene substance does not exist. The calculated energies of C_{120} (symm. C_6) and of C_{144} (symm. C_6) are also near the degenerate values.

According to our calculations the fullerenes C_n (with n more than 100) has the isomers with $DE < 0.2\text{eV}$. For example, C_{100} with the rotation axes C_2 ($DE = 0.12\text{eV}$), C_{110} with axes C_5 (0.12eV), and C_{112} (0.14eV).

For the fullerene C_{76} we verified the influence of the main diameters distortion. Molecule with one of the diameters 5% longer has DE 20% higher. For one of the diameter 5% shorter we obtain $DE = 0.8DE(\text{initial})$. But when all diameters are varied by 5% the value of band gap does not vary. It indicates that the shape of molecule is most important factor for gap variation.

For approximate evaluation of anisotropy we present the axes dimensions in X,Y,Z - directions for the coordinate system centered to the molecule mass center, and the axes directed along the main inertia moments. The comparison of isomers is made by the difference of atom coordinates lying on these axes.

It is necessary to mention that the calculated value of C_{60} gap is more than the experimental one, and that of C_{76} (symm.Td) is less than experimental value.

The results presented in Table 2 allow us to make the following conclusions.

1. Among the C_n isomers a molecule which is more spherical has more narrow spectral gap.

2. Among fullerenes with n more than 100 there are isomers with narrow band gap.

REFERENCES TO CHAPTER II

1. H.W.Kroto, J.R.Heath, S.C.O'Brien, R.F.Curl and R.E.Smalley, Nature, 318, 162 (1985).

Table 2. The results of C_n fullerene band gap calculations by the EHT.

Fullerene C_n	ΔE	Approximate symmetry			ΔE	Approximate symmetry		
	eV	Type	rotation ellipsoid diameter values, Å	Shape*	eV	Type	rotation ellipsoid diameter values, Å	Shape*
C_{60}	1.56	I_h	7.0 x 7.0 x 7.0	sph	-	-	-	-
C_{70}	1.58	D_{5h}	7.0 x 6.7 x 8.0	sph	-	-	-	-
C_{76}	1.17	D_2	6.6 x 7.5 x 8.7	-	0.21	T_d	7.7 x 7.9 x 7.8	sph
C_{78}	1.76	D_{3h}	7.1 x 7.1 x 8.6	-	1.23	C_2	7.0 x 7.3 x 8.5	-
C_{80}	0.0	D_{5h}	7.6 x 7.8 x 8.0	-	-	-	-	-
C_{84}	0.24	T_d	8.7 x 8.0 x 8.0	sph	-	-	-	-
C_{90}	1.31	D_5	10.3 x 6.8 x 6.8	/	-	-	-	-
C_{92}	0.61	D_5	7.2 x 8.0 x 9.0	-	0.26	C_2	9.0 x 9.0 x 8.6	sph
C_{96}	0.57	D_{3h}	8.0 x 8.0 x 9.9	-	-	-	-	-
C_{100}	1.28	D_5	6.8 x 6.9 x 11.5	/	0.12	C_2	7.7 x 9.3 x 10.0	-
C_{104}	0.73	D_{2h}	6.5 x 9.5 x 11.7	●	0.26	C_3	8.4 x 8.3 x 10.4	-
C_{108}	1.13	C_3	11.0 x 8.4 x 8.0	-	0.6	C_2	8.3 x 7.5 x 10.7	-
C_{110}	0.40	D_{5h}	12.8 x 6.7 x 6.9	/	0.12	D_5	10.4 x 10.2 x 8.6	●
C_{112}	0.14	C_2	7.6 x 9.0 x 10.8	●	-	-	-	-
C_{114}	1.50	D_{3h}	7.0 x 7.2 x 12.8	/	-	-	-	-
C_{116}	0.41	O_h	10.0 x 10.0 x 10.8	sph	-	-	-	-
C_{120}	1.59	C_5	11.0 x 11.0 x 8.2	●	0.02	C_6	9.5 x 9.5 x 8.8	-
C_{124}	0.51	C_2	8.4 x 8.6 x 13.8	/	-	-	-	-
C_{144}	0.01	C_6	9.4 x 10.8 x 9.3	-	-	-	-	-

*The molecular shapes are written as follows: **sph** means a spherical molecular shape, / does a lengthened ellipsoid, ● does a flattened one. The shapes were known from molecular sizes along the inertia momentum axes.

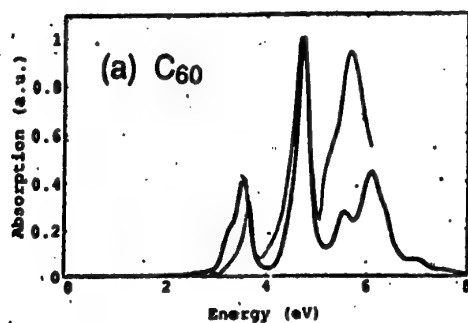


Fig 20. Optical absorption spectra for C₆₀ shown in arbitrary units. Experimental data are shown by thin line. They are taken from ref.2.

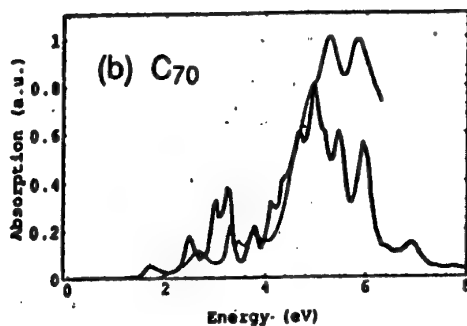


Fig 21. Optical spectra for C₇₀. Experimental data are shown by thin line. They are taken from ref.1.

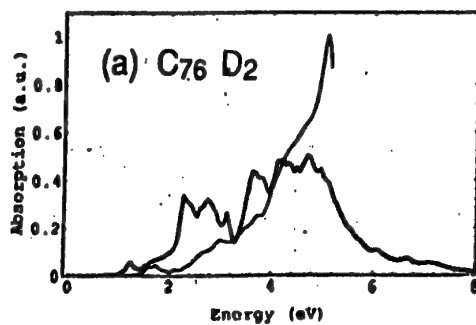
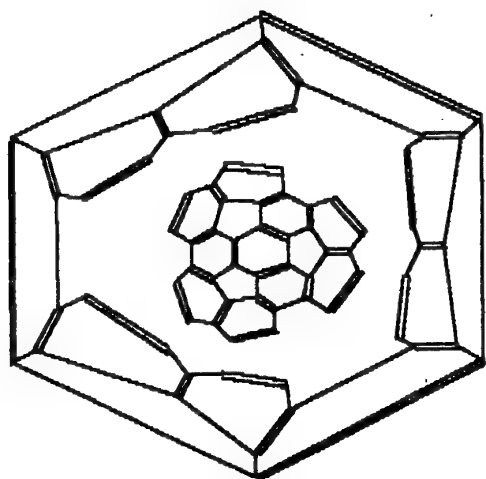
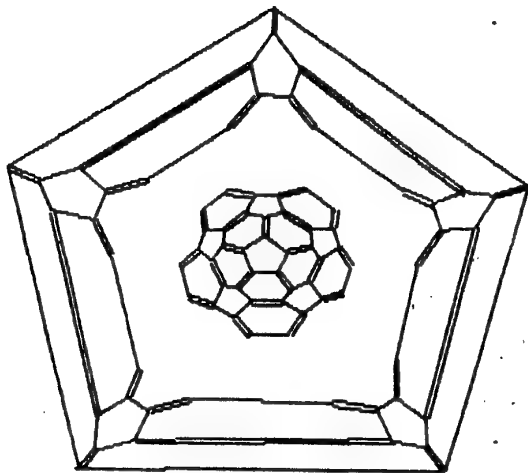


Fig 22. Optical absorption spectra for C₇₆ with D₂ symmetry, shown in arbitrary units. Experimental data are shown by thin line. They are taken from ref.5.



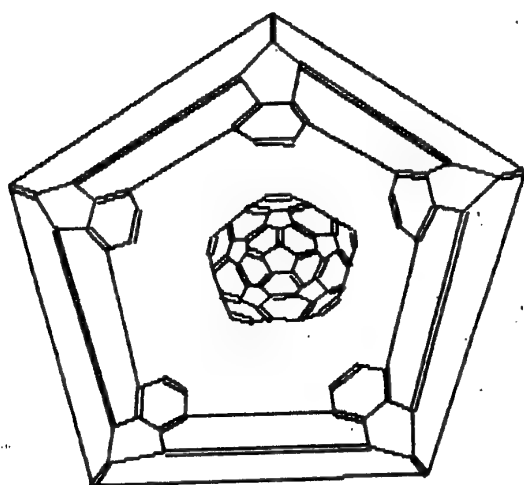
$$2 * C_{36} \quad (C_3)$$

Fig 23. Flat diagram of two fragments C₃₆ with symmetry C₃ that was used for our calculations.

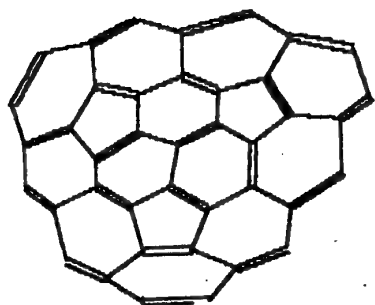


$$2 * C_{40} \quad (C_5)$$

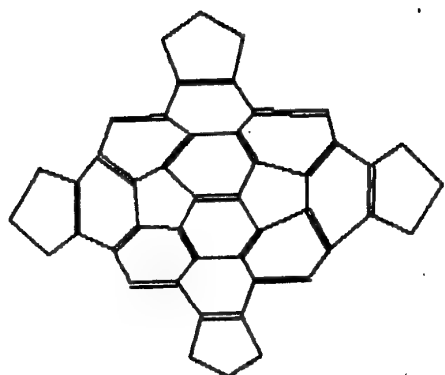
Fig 24. Flat diagram of two fragments C₄₀ with symmetry C₅ that was used for our calculations.



$2 * C_{50}$ (C_5)



C_{40} (C_3)



(C_{46}) (C_2)

Fig 25. Flat diagram of connection of two fragments C_{50} with symmetry C_5 and fragments C_{40} (symm. C_3) and C_{45} (symm. C_2) that were used for our calculations.

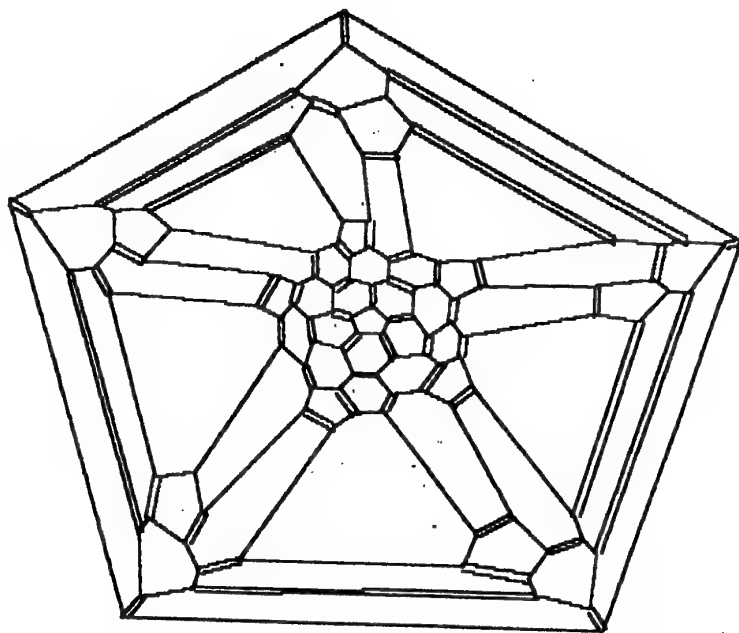


Fig.26. Flat diagram of two fragments C55 that was used for the construction of C110 fullerene.

C_{70} (D_{5h})

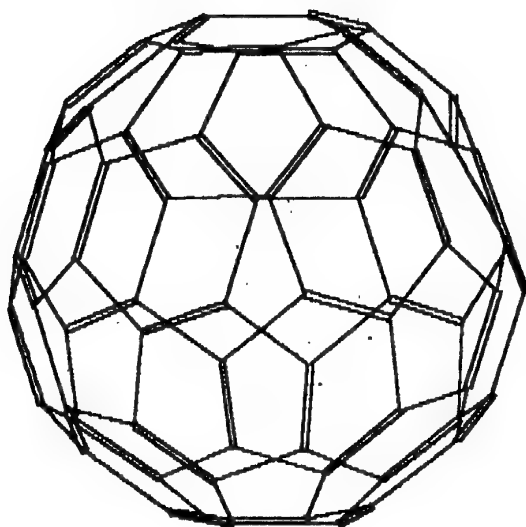


Fig 27. Molecular structure for C_{70} with D_{5h} symmetry.

C_{60} (I)

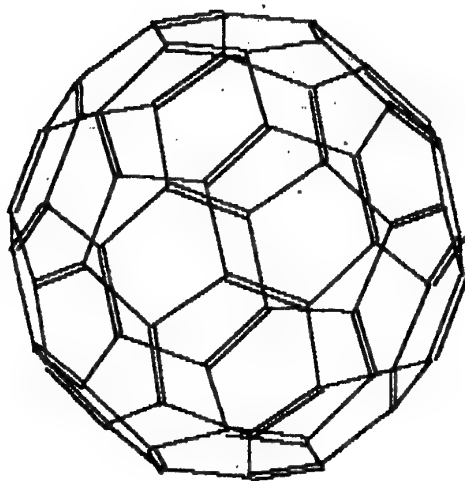


Fig 28. Molecular structure for C_{60} with I_h symmetry.

C_{76} (D_2)

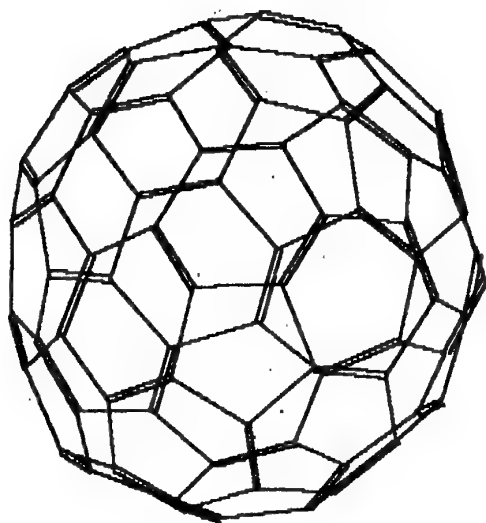


Fig.29. Molecular structure for C_{76} with D_2 symmetry.

C_{76} (T_d)

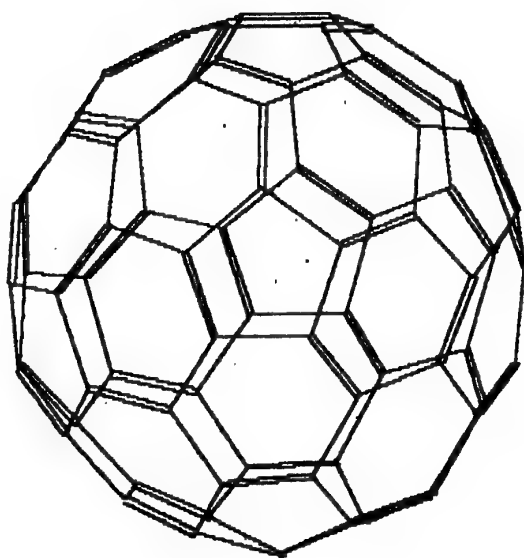


Fig.30. Molecular structure for C_{76} with T_d symmetry.

C_{78} (D_{3h})

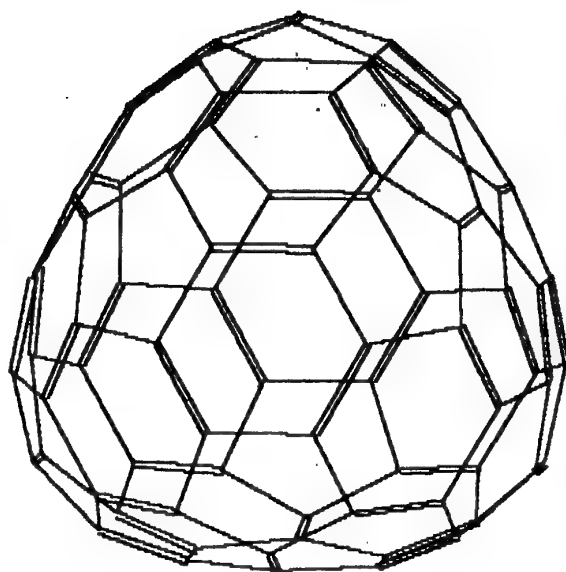


Fig.31. Molecular structure for C78 with D3h symmetry.

C_{78} (C_2)

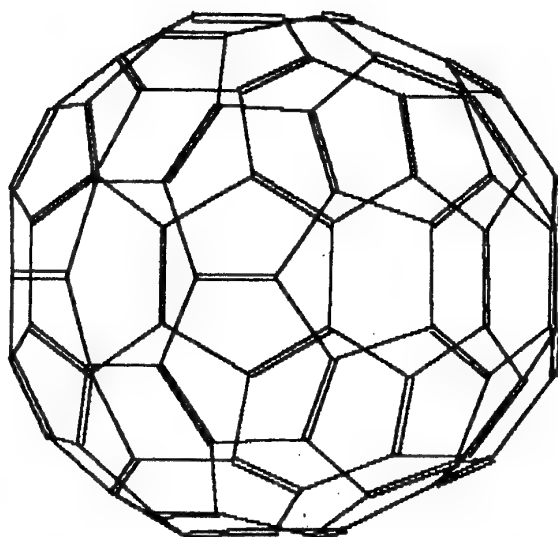


Fig.32. Molecular structure for C78 with C2 symmetry.

C_{96} (D_{3h})

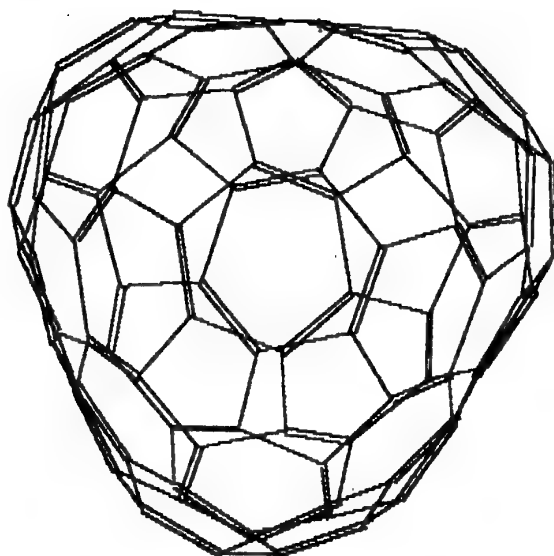


Fig. 33. Molecular structure for C₉₆ with D_{3h} symmetry.

C_{84} (T_d)

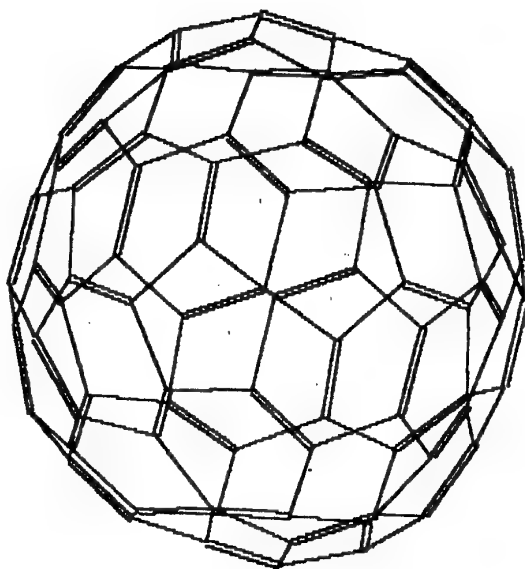


Fig. 34. Molecular structure for C₈₄ with T_d symmetry.

C_{90} (D_5)

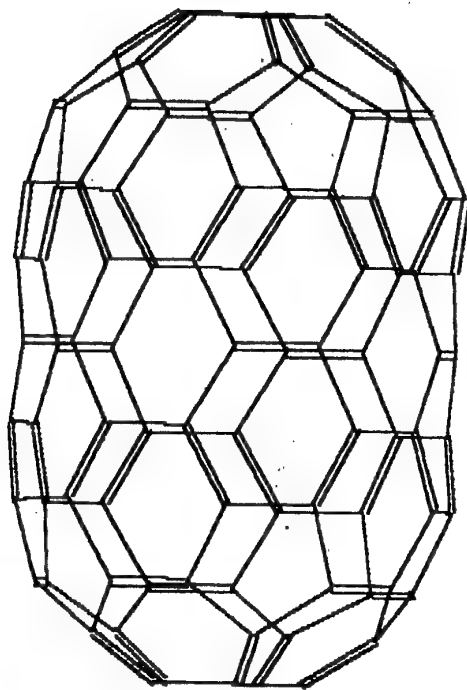


Fig.35. Molecular structure for C₉₀ with D₅ symmetry.

C_{112} (C_2)

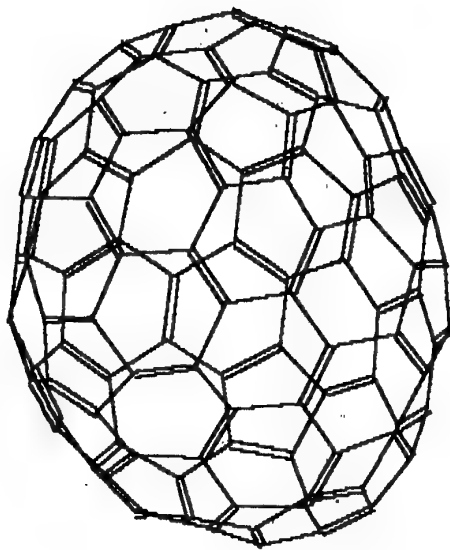


Fig.36. Molecular structure for C₁₁₂ with C₂ symmetry.

C_{92} ("")

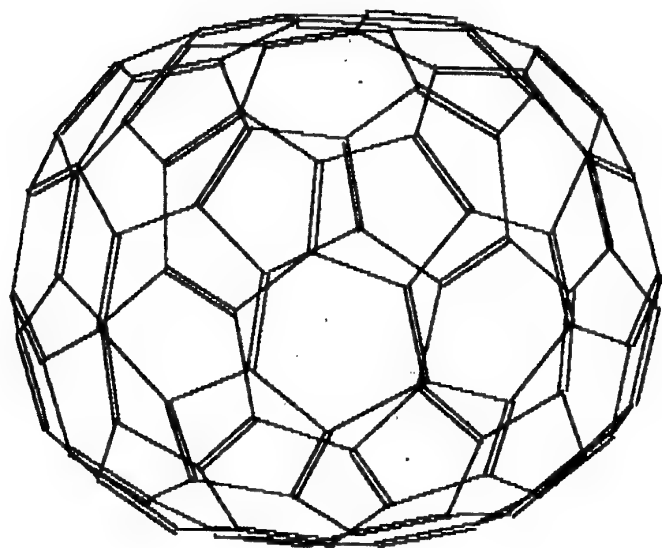


Fig.37. Molecular structure for C_{92} .

C_{92} (C_2)

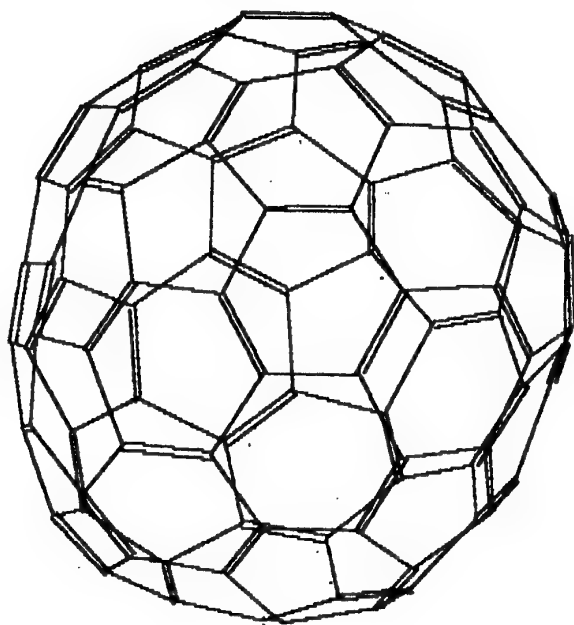


Fig.38. Molecular structure for C_{92} with C_2 symmetry.

C_{100} (D_5)

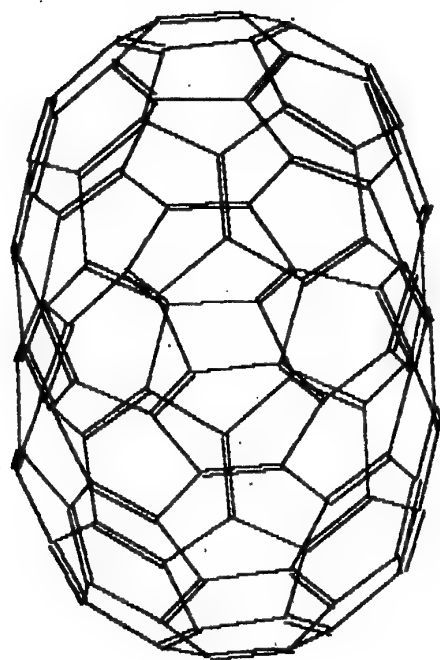


Fig.39. Molecular structure for C_{100} with D_5 symmetry.

C_{100} (C_2)

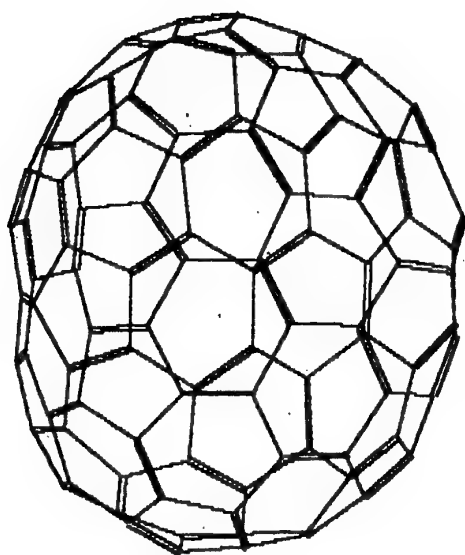


Fig.40. Molecular structure for C_{100} with C_2 symmetry.

C_{104} (D_{2h})

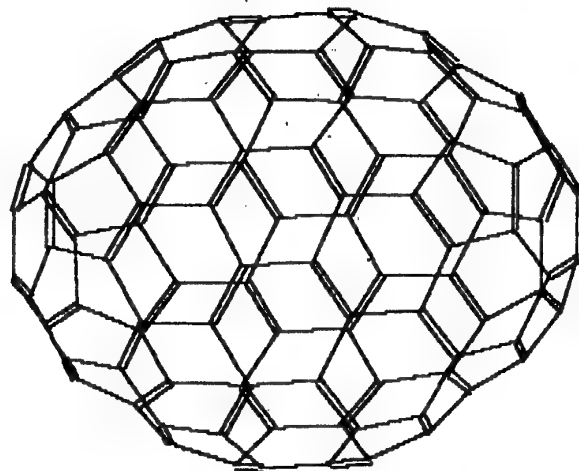


Fig.41. Molecular structure for C₁₀₄ with D_{2h} symmetry.

C_{104} (C_3)

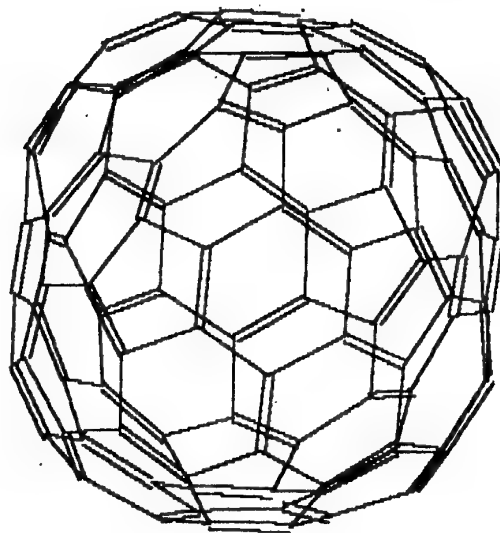


Fig.42. Molecular structure for C₁₀₄ with C₃ symmetry.

C_{108} (C_3)

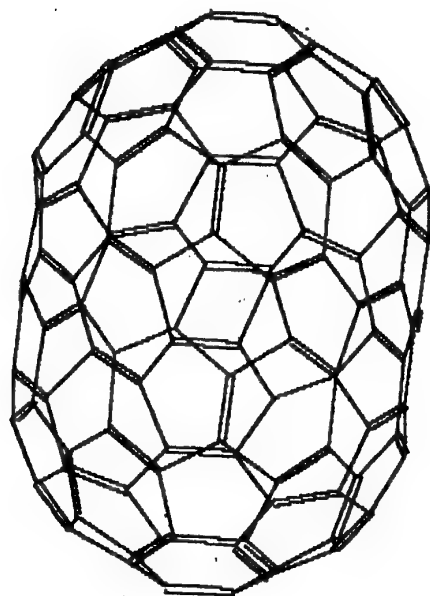


Fig.43. Molecular structure for C₁₀₈ with C₃ symmetry.

C_{108} (C_2)

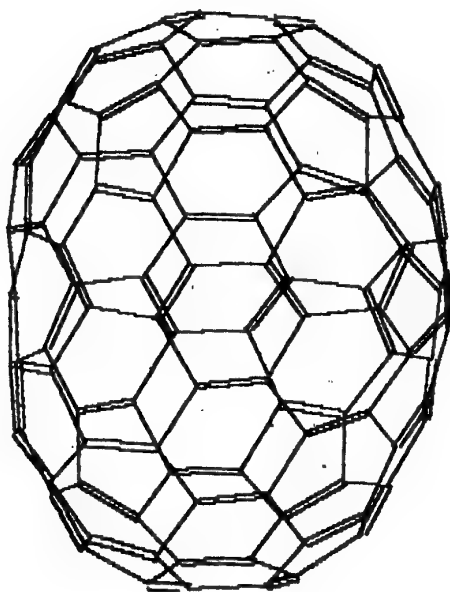


Fig.44. Molecular structure for C₁₀₈ with C₂ symmetry.

C_{110} (D_{5h})

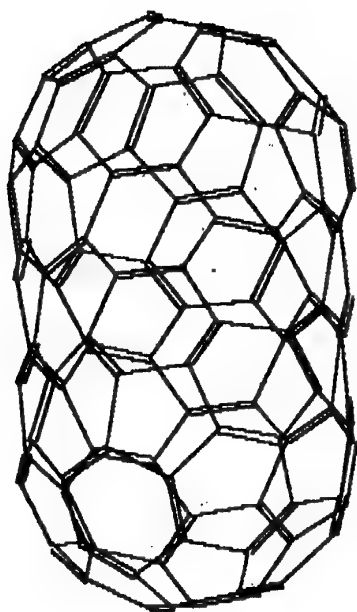


Fig.45. Molecular structure for C₁₁₀ with D_{5h} symmetry.

C_{110} (D_5)

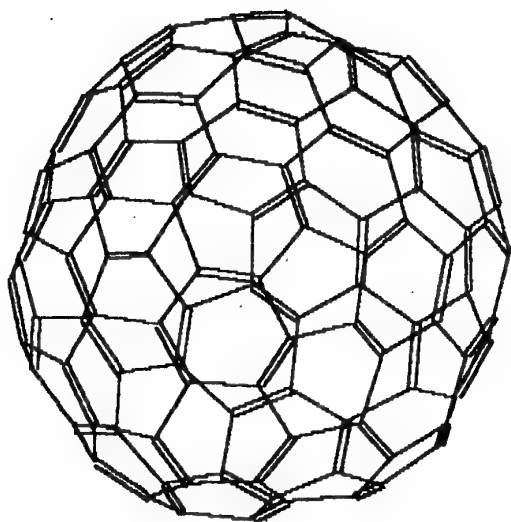


Fig.46. Molecular structure for C₁₁₀ with D₅ symmetry.

C_{124} (C_2)

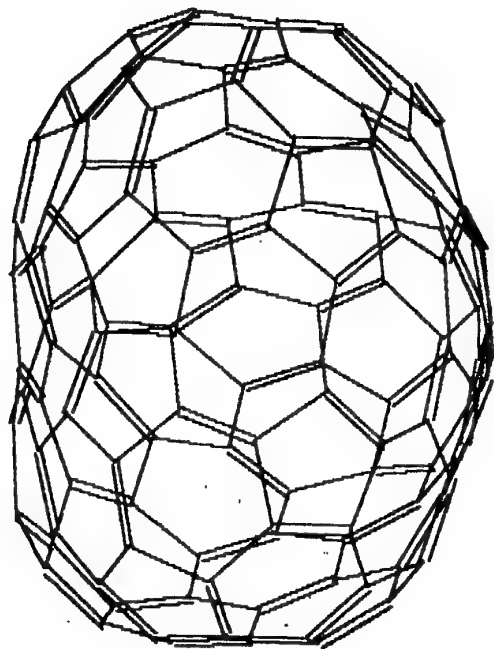


Fig.47. Molecular structure for C₁₂₄ with C₂ symmetry.

C_{114} (D_{3h})

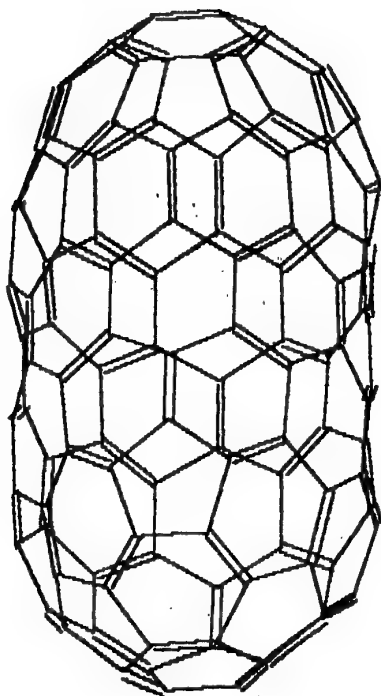


Fig.48. Molecular structure for C₁₁₄ with D_{3h} symmetry.

C_{120} (C_5)

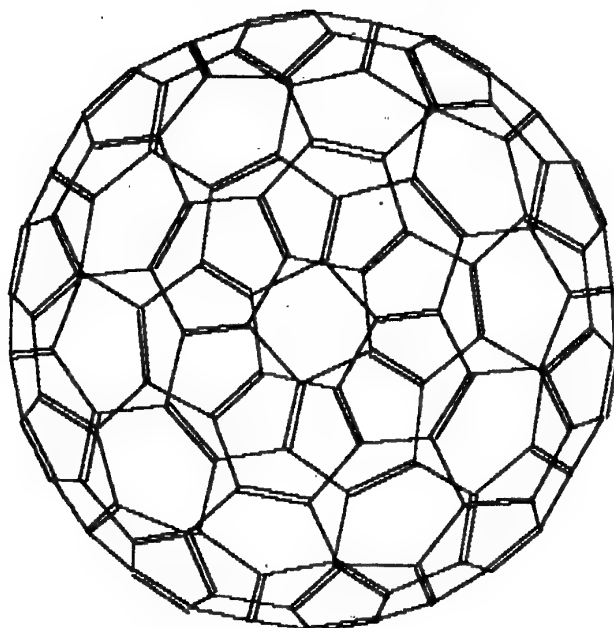


Fig.49. Molecular structure for C_{120} with C_5 symmetry.

C_{120} (C_6)

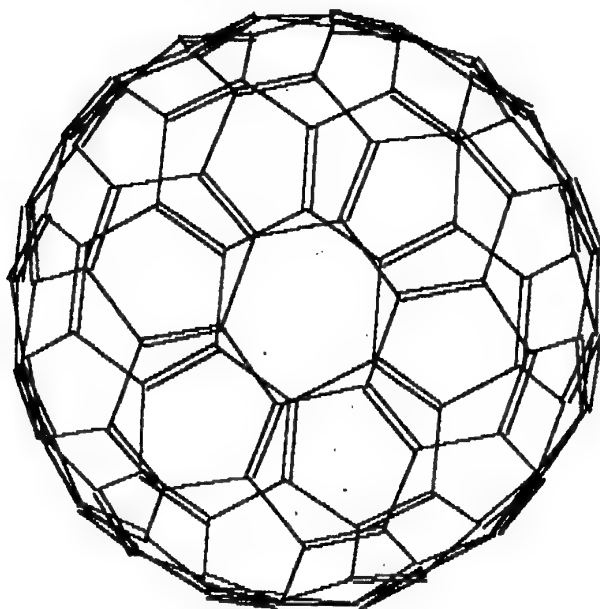


Fig.50. Molecular structure for C_{120} with C_6 symmetry.

C_{144} (C_6)

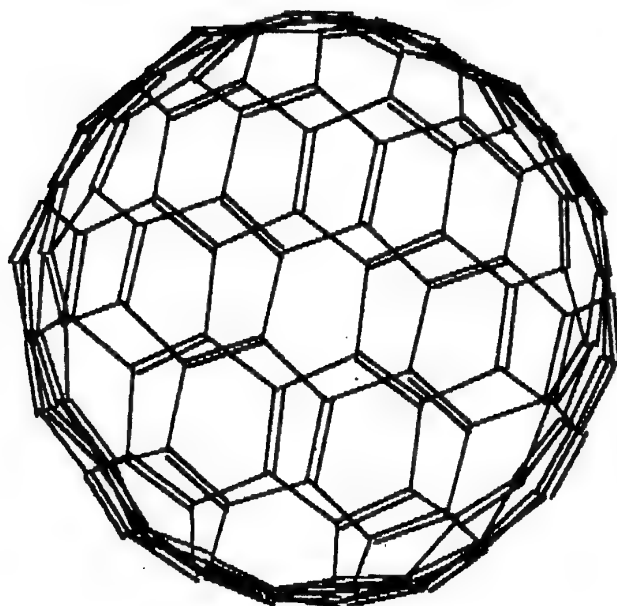


Fig.51. Molecular structure for C_{144} with C_6 symmetry.

C_{116} (O_h)

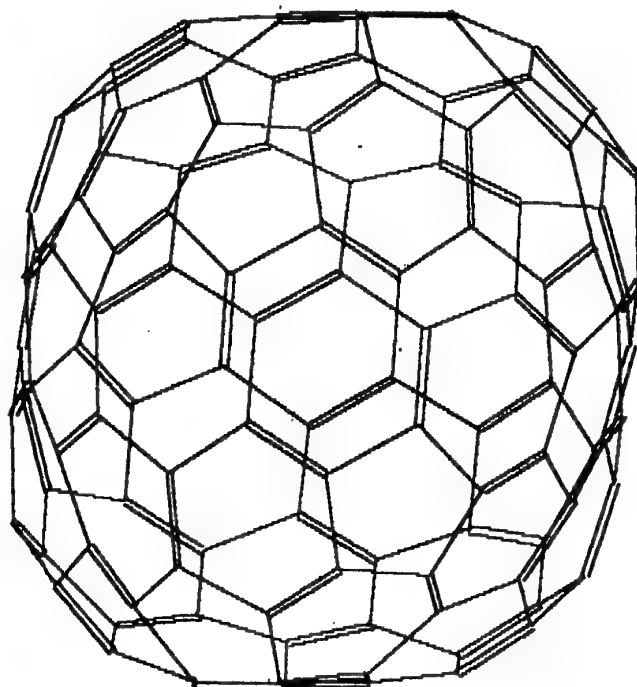


Fig.52. Molecular structure for C_{116} with C_2 symmetry.

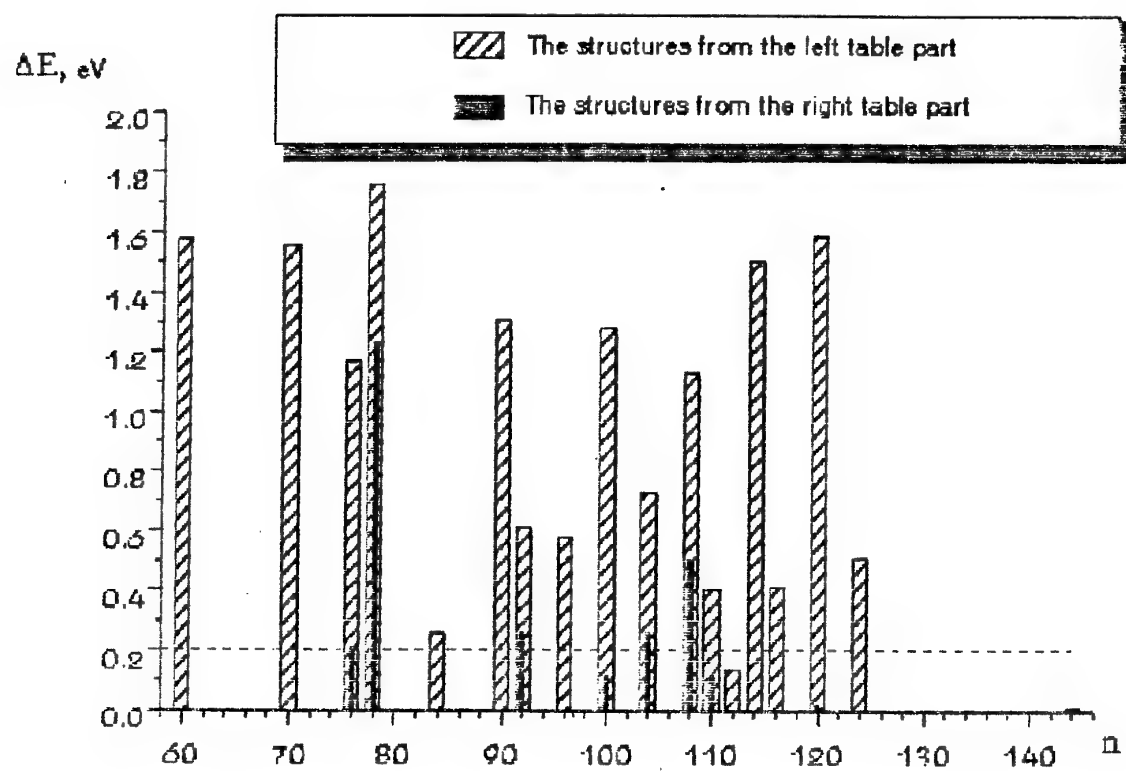


Fig. 53. Calculated band gap energies of high fullerenes.

2. S.L. Ren, Y. Wang, A.M. Rao, E. McRae, J.M. Holden, T. Hager, Kai An Wang, W.T. Lee, H.F. Ni, J. Selegue and P.C. Eklund, Appl. Phys. Lett., 197, 2678 (1991).
3. J.S. Meth, H. Vanherzeele and Y. Wang, Chem. Phys. Lett., 197 (1992)
4. Z.H. Kafafi, J.R. Lindle, R.G.S. Pong, F.J. Bartolli, L.J. Lingg and J. Milliken, Chem. Phys. Lett., 188, 492 (1992).
5. R. Ettl, I. Chao, F. Diederich and R.L. Whetten, Nature, 353, 149 (1991).
6. K. Kikuchi, N. Nakahara, T. Wakabayashi, M. Honda, H. Matsumiya, T. Morivaki, S. Suzuki, H. Shiromaru, K. Saito, K. Yamauchi, I. Ikemoto and Y. Ashiba, Chem. Phys. Lett., 188, 177 (1992).
7. K. Hargaya and S. Abe, Jpn. J. Appl. Phys., 31, L887 (1992).
8. K. Hargaya and S. Abe, J. Lumin., 20, 187 (1994).
9. K. Hargaya, Jpn. J. Appl. Phys., 33, L786 (1994).
10. Au Chin Tang, Fu Quang Huang, Quan Shu Li, Ruo Zhuang Liu, Chem. Phys. Lett., 227, 579 (1994).

III. OPTICAL AND INFRARED SPECTROSCOPY OF FULLERENES

Since the discovery of fullerenes [1], their spectroscopic properties have been extensively studied both theoretically and experimentally. The optical spectra were discussed earlier, and we do not repeat them. We shall discuss the IR spectrometry of fullerenes as compared to our experimental data.

Experimental part

Fullerene synthesis

To synthesize fullerenes we use the evaporation of high purity carbon by DC arc discharge source. This method produces carbon soot from which the fullerenes are extracted by use of appropriate solvent. The arc discharge process is more efficient than others. The apparatus after pump-down of chamber is isolated from the pump and then backfilled with high purity

helium to a pressure of 200 Torr. The production of fullerenes is carried out within the water-cooled region. The power supply is a regulated 500 A, 80-V DC power supply. We adjust the gap between the electrodes to attain maximum brightness of the plasma. Under these conditions the plasma draws 400-500 A from power supply. At the end of a run, the apparatus is filled to atmospheric pressure with He. The chamber is then opened and the soot scraped from the shims and collected for further purification. With this method, tens of grams of soot (that contain high fullerenes) per day can be produced.

Mass spectrometry

We use laser desorption time-of-flight (TOF) mass spectrometer (LAMMA-1000). The experiment measures the mass spectrum of negative ions or positive ions emitted directly from the sample in the desorption process. The mass resolution of the apparatus is usually 400 under these experimental conditions. The base pressure of the system is typically 2×10^{-10} Torr. Neutral and ionized fullerene clusters are desorbed from glass substrate by 532 nm light. The fluence of the desorption laser is held constant at approximately 10-100 mJ/cm², which is just above the threshold for ion production. The laser desorption at these intensities produces a minimum of fragmentation of the desorbing fullerene molecules. However, at slightly higher intensities, significant fragmentation occurs.

Extraction and separation of the fullerenes

In the first stage of this work extraction was performed with chloroform by stirring a portion of the soot in warm solvent for one hour. Filtration of this mixture yields a dark red solution indicating the presence of C₆₀ and C₇₀ and small amounts of higher fullerenes. We analyzed this solution by TOF mass spectrometer measurements in following procedure. A small amount of solution was evaporated onto sample holder and laser TOF mass spectrometric measurements were performed on the residue. The TOF mass spectrum of this sample showed primarily C₆₀ and C₇₀ with small amount of C₇₈ and C₈₄.

C_{60} was purified by medium-pressure chromatography from first chloroform extract. TOF mass spectrometry, chromatography showed better than 99.6% purity of the resulting material used for preparation of films. IR-measurements of solution were made on C_{60} with quality 99.9%.

C_{70} was purified by medium-pressure chromatography from first chloroform extract. TOF mass spectrometry, chromatography and spectrophotometry showed better than 99% purity of the resulting material.

In the second stage we extracted high fullerenes by toluene. We performed this extraction on soot previously extracted with chloroform to deplete the soot of C_{60} and C_{70} . The solution was evaporated onto substrate and examined by TOF MS. The result is shown in Fig.54. Along with C_{60} and C_{70} a significant number of high fullerenes were also observed in the mass spectrum.

C_{76} was purified by medium-pressure chromatography from toluene extraction. TOF mass spectrometry showed better than 85% purity of the resulting material (the main admixture is C_{84}).

We used, in our experiments, a mixture of high fullerenes that was prepared by sixth extraction after successive five extractions of fullerenes from the soot. TOF MS of such mixture is presented in Fig.55. It can be seen from the distribution of concentrations for this mixture that quantities of C_{60} and C_{70} are lower than for the mixture, extracted by xylene at high pressure, and the distribution has maximum in desired for us (from previous calculations) band of masses. Therefore we use it for optic absorption experiments.

Additionally, we have extracted giant fullerenes with xylene at high pressure. We repeated the experiment first reported by the group at Arizona [2] where toluene in a bomb reactor at high temperature and pressure was used to extract soot that had been previously extracted with toluene to deplete the soot of C_{60} and C_{70} . We performed this procedure on soot previously extracted by toluene in Soxhlet. The result of TOF MS is shown in Fig.56. High quantity of giant fullerenes (to C_{250}) are

presented in mass spectrum, but we do not observe masses as high as reported previously, probably due to difference in experimental conditions of temperature and pressure. It is interesting to mention that once extracted from the soot, the fullerenes can be redissolved in lower boiling solvents.

Optic absorption experiments

We made UV-, IR- and optic spectra of fullerenes in toluene solution and of fullerene films on silicon substrate. Films were prepared by evaporation of fullerene in high vacuum at 400C or from the fullerene solution that was sputtered on rotated monocrystalline silicon substrate.

All measurements in UV-, optic band and near IR were made on spectrometer SPECORD and SF-26.

Infrared spectra were taken with Perkin Elmer IR spectrometer model 883 in transmission mode using a Ge bolometer in far infrared and an MCT detector in mid-infrared at room temperature on fullerene with the Si plate as reference and on fullerenes solutions relatively solvent.

Results and discussion

Optic- and UV-absorption measurements

In Figs.57 and 58 are presented near UV-, optic spectra of C_{60} 0.1 mg/ml solution in toluene. One can see the characteristic peaks of C_{60} (one of them at 406nm) that are distributed in the near UV- and optic bands, and the absence of C_{70} intensive peak at 475nm. The optic absorption of solution goes to 0 at 620-660 nm.

The fullerene C_{60} film absorption spectrum is presented in Fig.59. The film thickness permits one to resolve the peak in near UV-band at 340nm. Absorption goes to 0 at 620-660nm (16000- 15000cm⁻¹).

Figures 60 and 62 represent the spectra of C_{70} toluene solution that are typical of this fullerene, and have the characteristic peaks at 335, 365, 385 and 475nm (29700, 27300,

26100, 21000cm⁻¹) that are distributed in near UV- and optic bands, and the absence of C₆₀. The optic absorption of solution goes to 0 at 620-660nm.

Optic absorption spectrum of C₇₆ solution (Fig.58) differs from the lower fullerenes by elevated absorption in near IR band (to values more than 800nm). This indicates that dislocation of absorption to the near IR band for the high fullerenes occurs. One can see the admixture of C₇₀ (peaks at 26100cm and 21000cm⁻¹).

Solution of the first toluene extraction (Figs.63,64) has the peaks of C₆₀ (at 406nm) and C₇₀ (at 475nm), and a little absorption in near IR band (Fig.63). But the presence of elevated quantities of C₆₀ and C₇₀ in mixture inhibits this phenomenon.

For solution of the sixth extraction (Fig.63) it is impossible to detect the characteristic peaks of the lower fullerenes. The tail of absorption spectrum goes to IR band without outstanding parts. This corresponds to a superposition of absorption spectra for many fullerenes with near equaled concentrations (as can be seen from TOF MS).

The IR absorption measurements

IR spectra of C₆₀ solution, film and mixture with KBr

The exceptional symmetry of the C₆₀ molecule was first revealed by infrared spectrum [3], consisting of only four lines (the four F(1u) modes required by the selection rule for the I(h) point group of the truncated icosahedron). This spectrum was predicted for the isolated molecule; in the solid state, where the local symmetry is lowered, one would expect splitting of degenerate modes as well as activation of forbidden molecular vibrations. At room temperature these effects are weak, due to the dynamic orientational disorder of the almost freely rotating C₆₀ balls. However, under the orientational phase transition temperature 250K [4] the rotation becomes

hindered, and there are four unequivalent molecules in the unit cell, differing in their orientations. The molecules do not leave their close-packed fcc positions, but the structure can now be regarded as four interpenetrating simple cubic sublattices, changing the space group from Fm3m to Pa3 [5].

A full group theoretical description of vibrational modes in different crystallographic environments was made by Dresselhaus et al. [6].

The transmission in IR band of C_{60} film is shown on Fig.66, that of C_{60} solution (with reference), in Fig.67, and that for C_{60} +KBr mixture, in Fig.68. The peaks at 525, 574, 1181 and 1428 cm belong to C_{60} (Fig.68; mixture C_{60} +KBr).

Due to the granular nature of the film (Fig.66), the scattering effects are important. The intensities deviate from different films, although the peak frequencies remain the same. There are also differences in the lineshapes of the low-frequency bands. For the weaker lines, however, the effects are far less dramatic.

The features at 1536 (Fig.68) and 2330 cm are seen in almost every spectrum published so far. They are linked to oxygen contamination. Werner et al. [7] have extensively studied the interaction of oxygen with C_{60} . According to their results, C_{60} adsorbs oxygen and CO_2 even in an inert gas atmosphere with impurity concentration as low as a few ppm. These molecules enter the C_{60} crystals in a clathrate-like fashion, with no chemical interaction, but oxygen may react furtherly forming an epoxy-type bond which can be changed into an aryl ether-type structure. In our spectra the 1348 cm peak attributed to the latter is missing (Fig.68).

The infrared spectrum of CO_2 is also known [8,9], and we can exclude its presence taking in to account the lack of lines between 770 and 800 cm (Fig.68; C_{60} +KBr).

The two modes in question could result from "clathrate-type" CO (2330cm [7]) and oxygen (1536 cm), respectively. For molecular oxygen, the stretching mode at 1555cm [10] is infrared inactive, but clathrate formation can change the charge dist-

tribution, and thus introduce a transition dipole moment for the stretching vibration.

Another characteristic region is that of C-H stretching vibrations around 3000 cm. Impurities containing C-H bonds tend to be common in C₆₀ films, and are usually attributed to solvent traces. Examining the spectral pattern of our films we conclude that the toluene is present in the films (Fig.66), and is absent in mixture C₆₀+KBr. The spectra lines at 1460 (C-H bend) and 1730 cm (aromatic ring vibration) can also be accounted for by assuming the presence of this precursor in film.

In solution we do not see these lines as we use solvent as the reference (Fig.67).

Higher fullerenes, above all C₇₀, are possible contaminants, but we did not observe the C₇₀ absorption lines at 642, 674 and 795 cm [11] in any of our samples.

Infrared spectra of C₇₀

Among the many stable fullerenes, C₇₀ is considered to be the second most stable molecule, following the C₆₀ molecule. The molecular structure of C₇₀ belongs to D_{5h} symmetry which consists of an elongated fivefold (C₅) axes, a five twofold (C₂) axes and a mirror plane (σ_h) perpendicular to the C₅ axis. According to group theory, there are 206 molecular vib-

rations in C₇₀ among which 31 are infrared-active [12]. However infrared modes with sufficient intensity are observed experimentally for only 16 modes. The assignment of the vibrational modes for C₇₀ is not well established presently though there are many theoretical calculations available for C₇₀ [12,13,14]. In Table 2, we list values of the frequency and relative intensity of the C₇₀ modes which are calculated by PM3 method. The IR-active vibrations whose frequencies are more than 1000 cm are basically (bond length) stretching vibrations and the vibrations with frequencies less than 1000 cm are (bond angle) deformation vibrations.

Table 2

Infrared-active modes sorted by its intensity.

Frequency	Intensity	Frequency	Intensity
1662	14.69	1277	0.57
922	2.37	474	0.55
1736	2.03	1069	0.48
1812	1.92	1614	0.47
1720	1.81	716	0.31
724	1.43	1500	0.31
612	1.32	1464	0.25
1345	1.18	1360	0.22
662	0.73	517	0.20

Experimental values of frequencies are : 1460, 1430, 1414, 1134, 795, 674, 642, 578, 565, 535, 458. It is clear that there exists a difference between the calculated and measured frequencies, and the relative intensities.

In Figure 62 we show the transmission of C_{70} solution in IR band. The film has a granular nature, and the scattering effects are also important. The intensities deviate for different films, although the peak frequencies remain the same. We observe in our samples the C_{70} absorption lines at 642, 674 and 795 cm^{-1} in [11].

Figures 69-71 represent the transmission of C_{70} +KBr, the first extraction of + KBr and the sixth extraction of + KBr mixtures that have the same features.

The near IR spectra of the first toluene extraction and the sixth extraction are presented in Figs.63-64. We do not see the electron absorption spectra for the wave length of 3000-5000 nm in our experimental data.

Two reasons could explain these results:

The mixtures obtained contain a small quantity of IR-active isomers (such as C_{100} with symm. C_2);

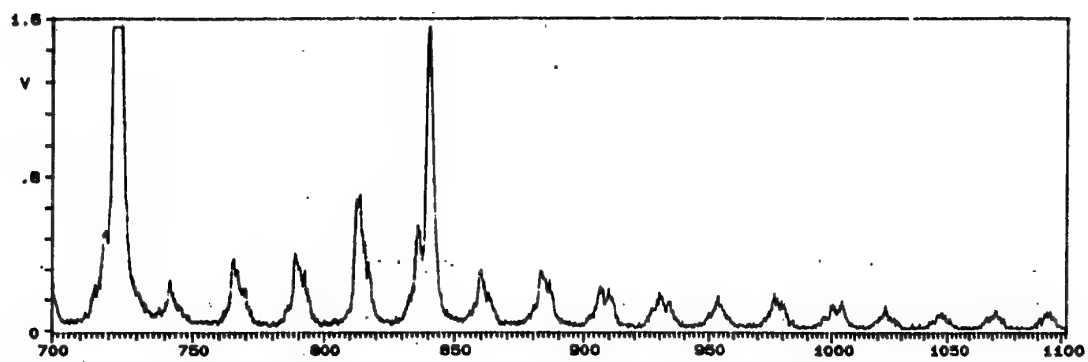


Fig.54. Mass spectrum of fullerene mixture extracted by toluene (first extract).

SPECTRUM 12280

15/ 2/ 1993

POLARITY +

LASER 00

RANGE .80 V

shoot 5.02

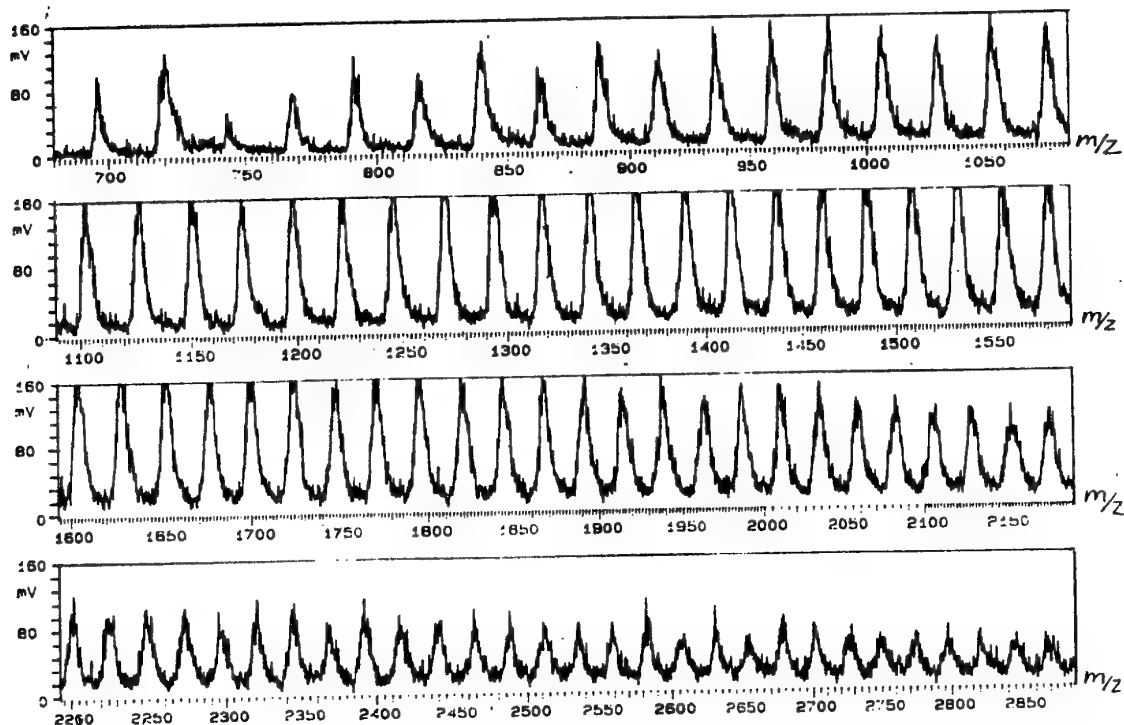


Fig.55 Mass spectrum of sixth toluene extract of fullerenes.

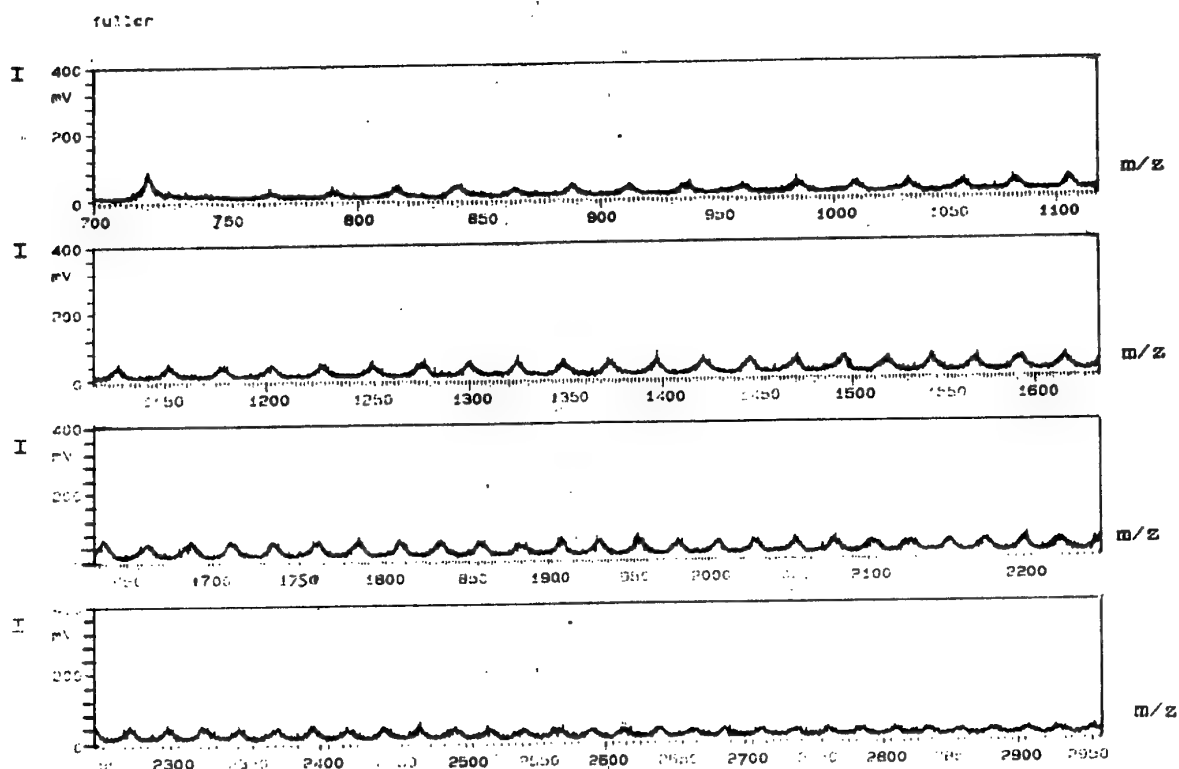


Fig.56 Mass spectrum of fullerene mixture extracted by xylene at high pressure and temperature.

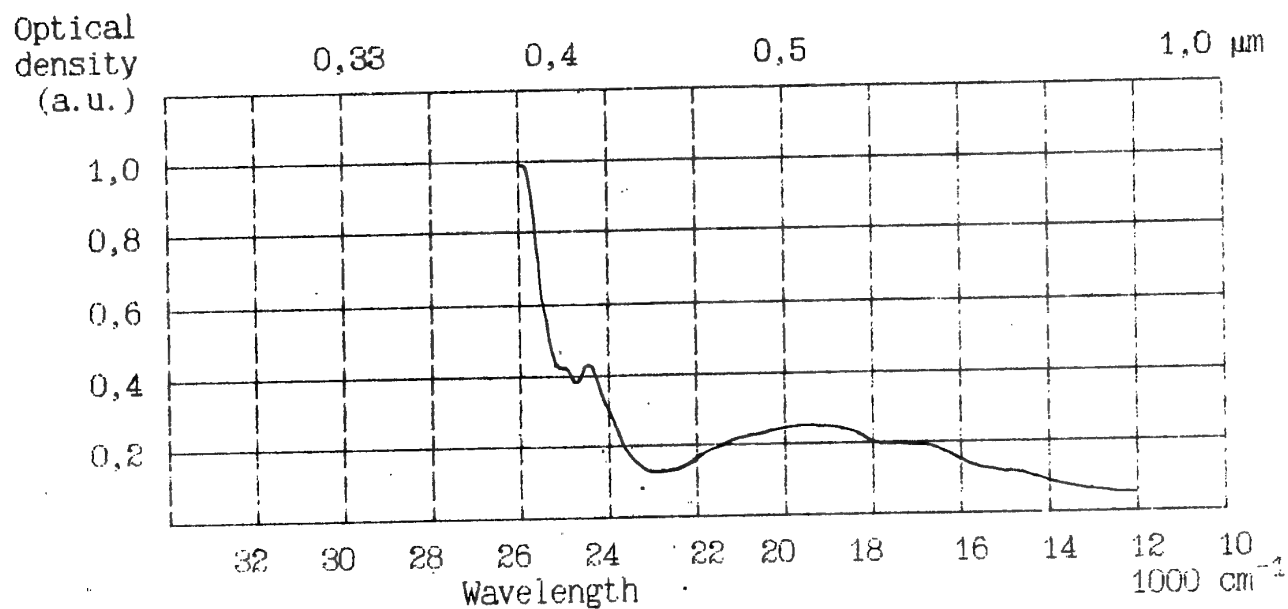


Fig. 57 Absorption spectrum of C₆₀ solution in toluene for visible and near-IR bands.

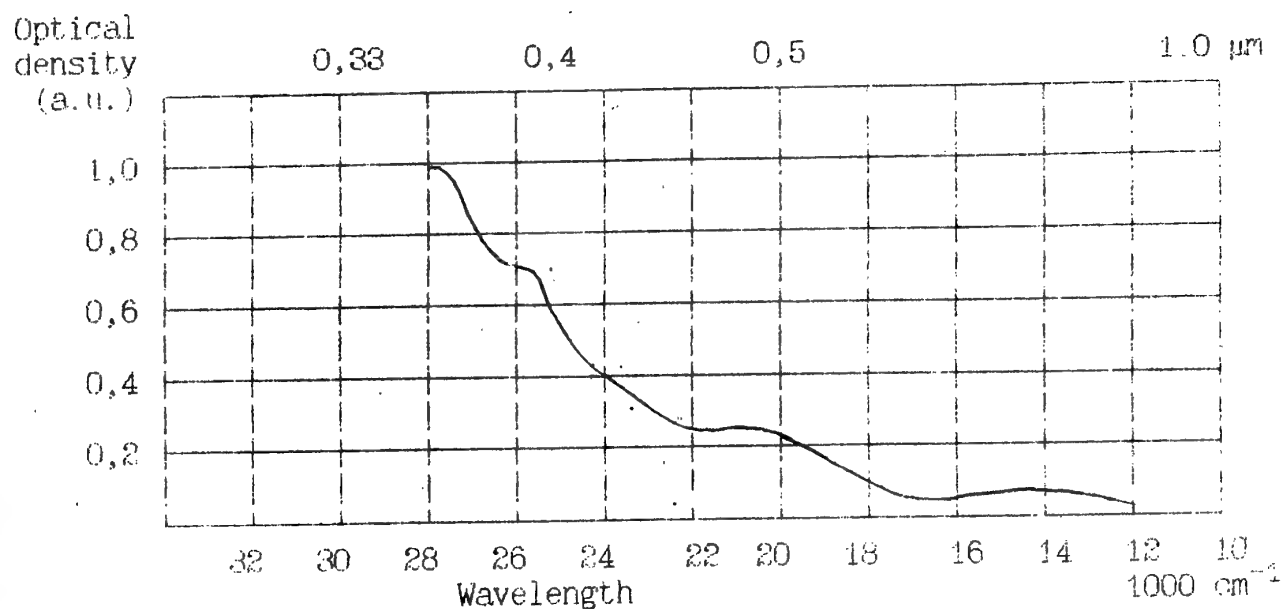


Fig. 58 Absorption spectrum of C₇₆ solution in toluene for visible and near-IR bands.

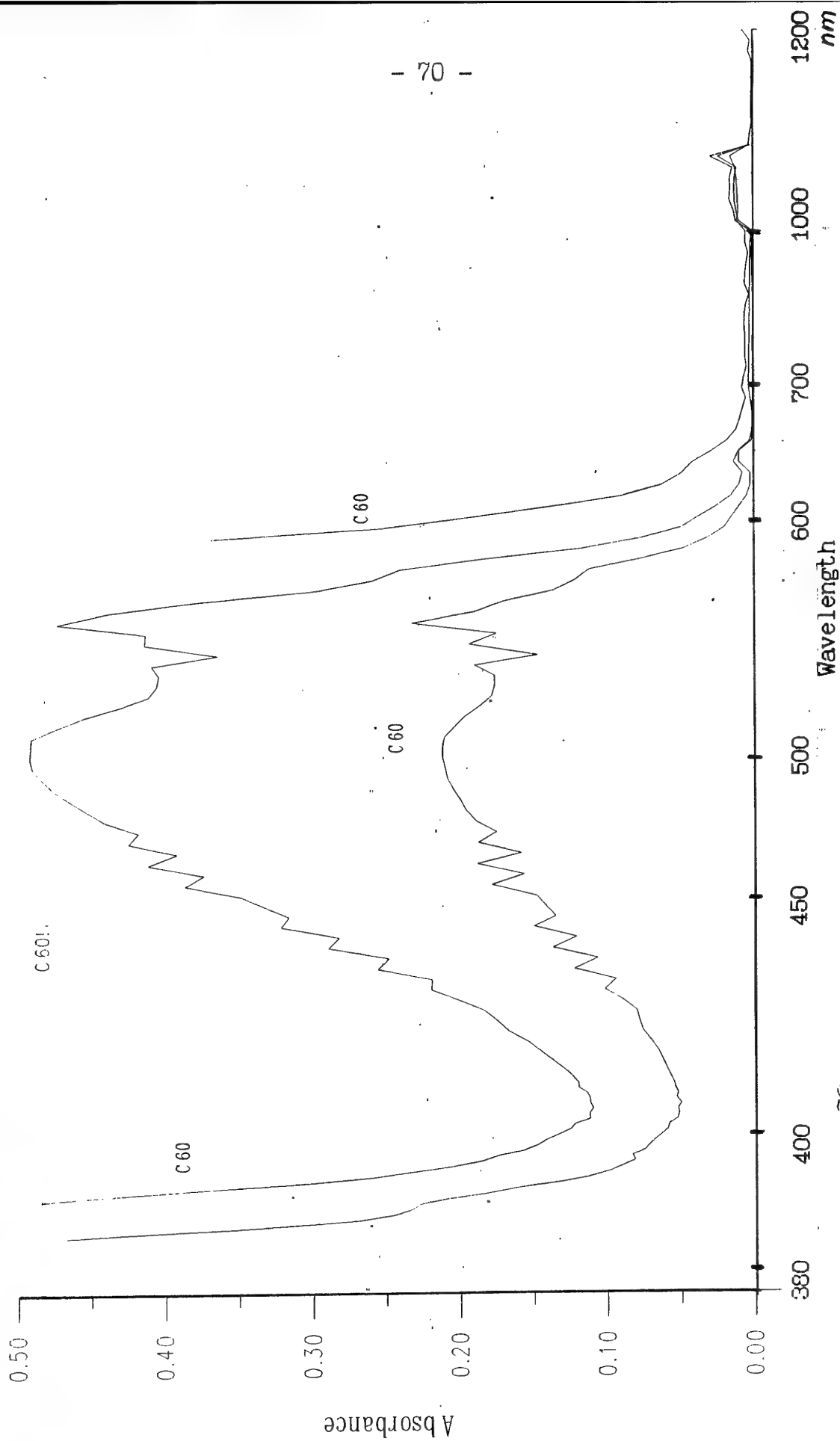


Fig. 59 UV-optic absorption of C₆₀ solution.

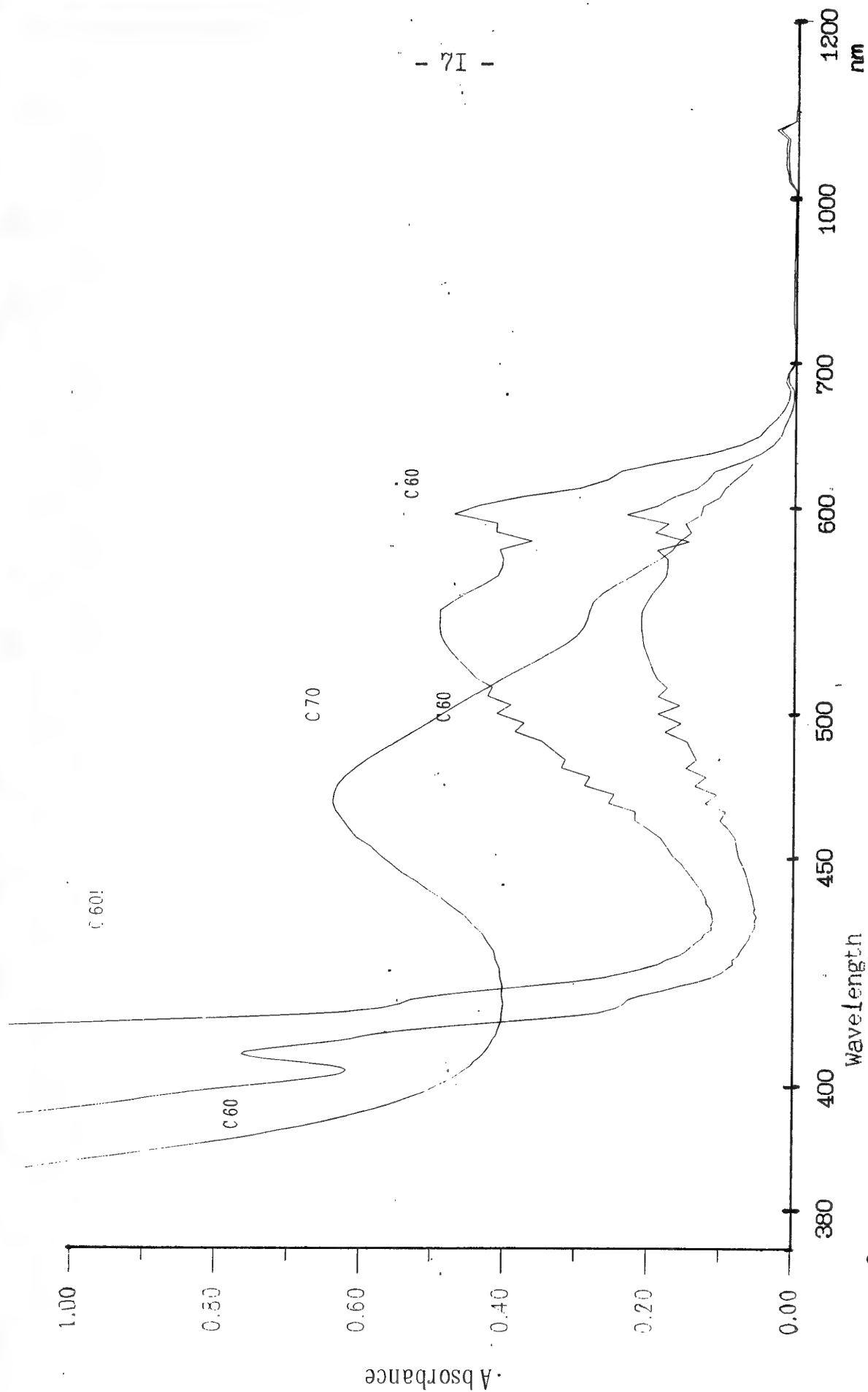


Fig. 60 Comparison of UV-Vis optic absorption spectra of C₆₀ and C₇₀ in toluene solution.

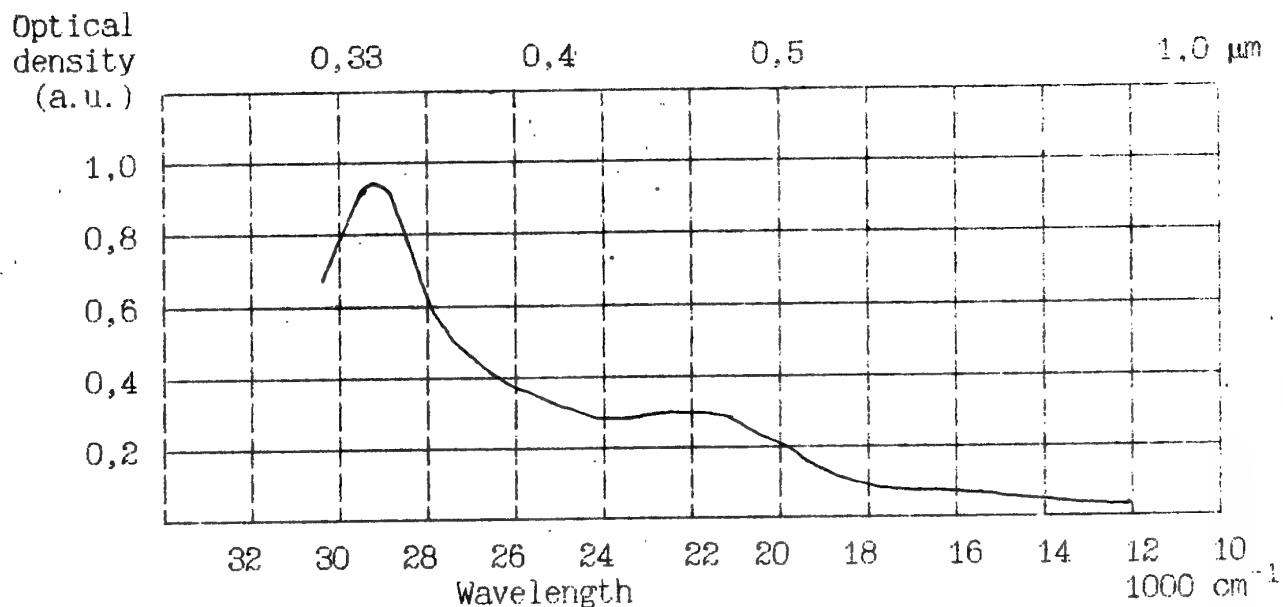


Fig. 61 The absorption spectrum of C₆₀ film evaporated on monocrystalline aluminium oxide substrate in comparison to aluminium oxide one in UV, visible and near IR bands.

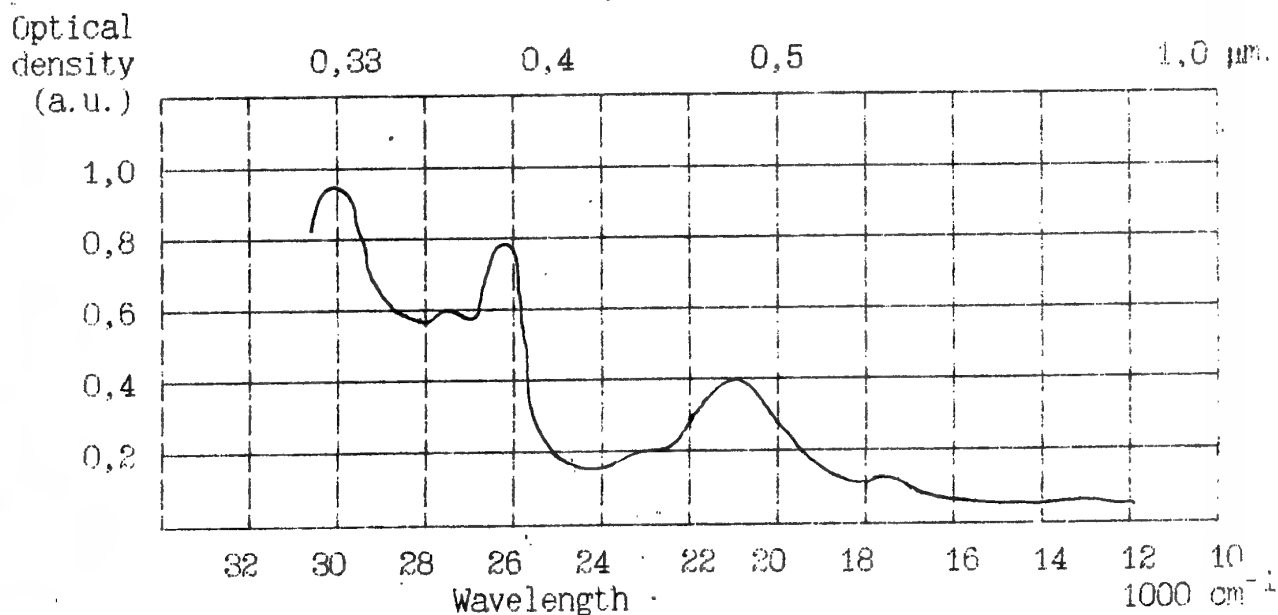


Fig. 62 Absorption spectrum of the C₇₀ solution in toluene for UV, visible and near IR bands.

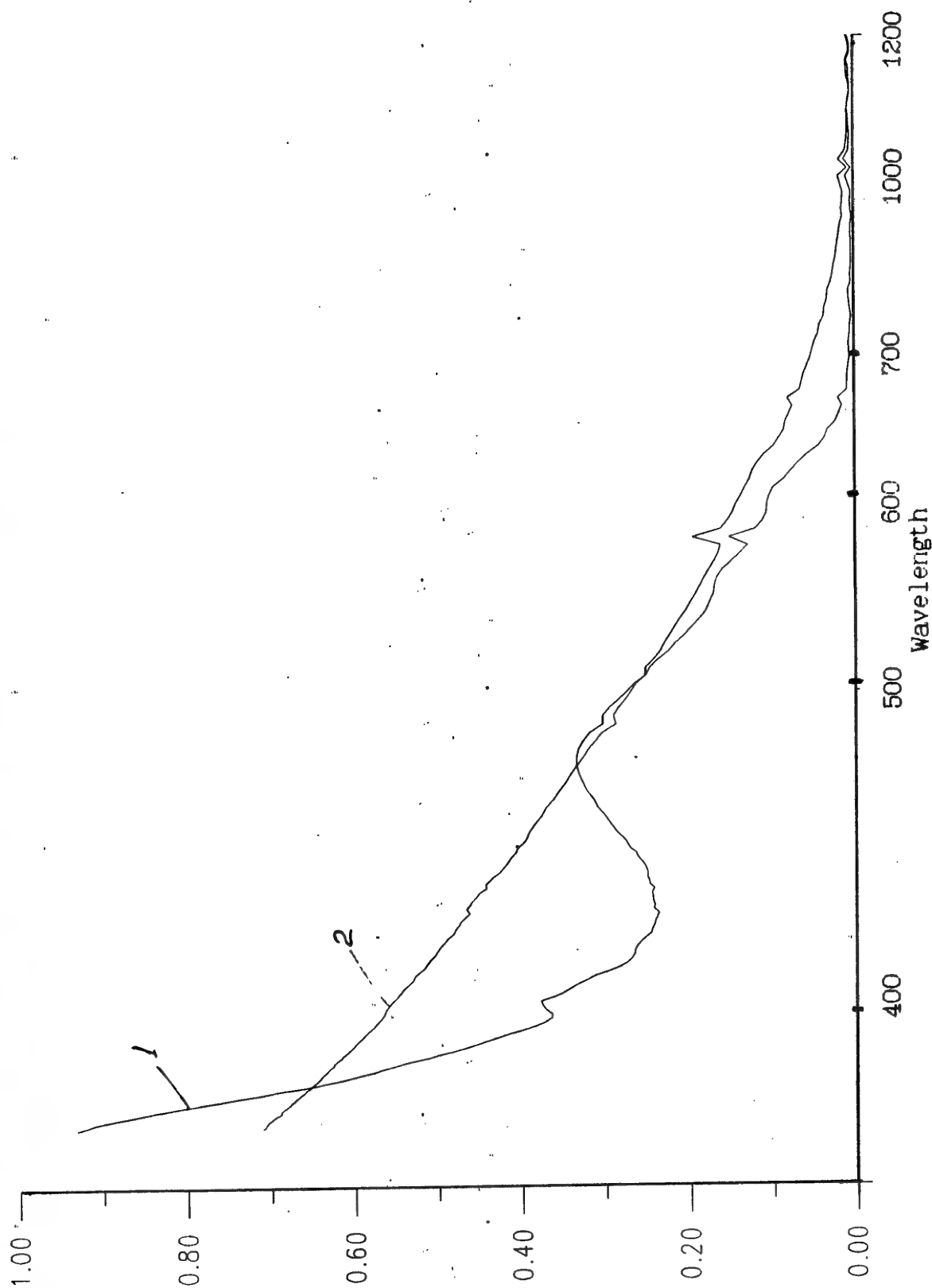


Fig 63 Comparison of absorption spectra of first (1) and sixth (2) toluene extractions.

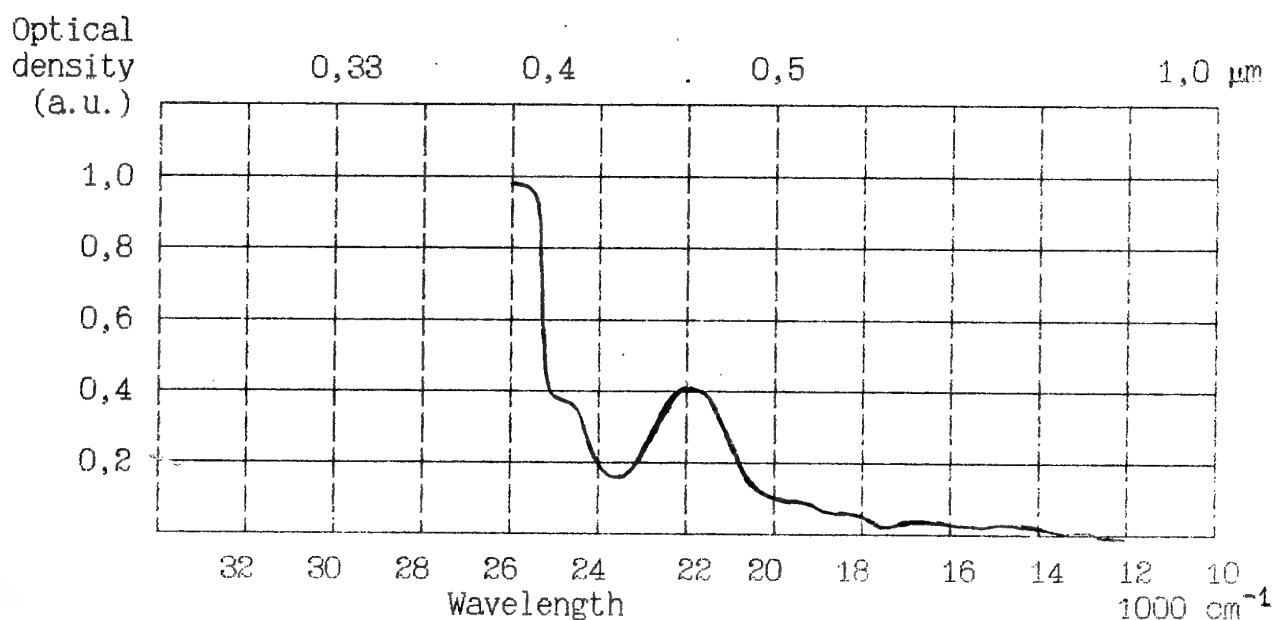


Fig. 64 Absorption spectrum of C₆₀-C₁₅₀ mixture solution in toluene for visible and near-IR bands.

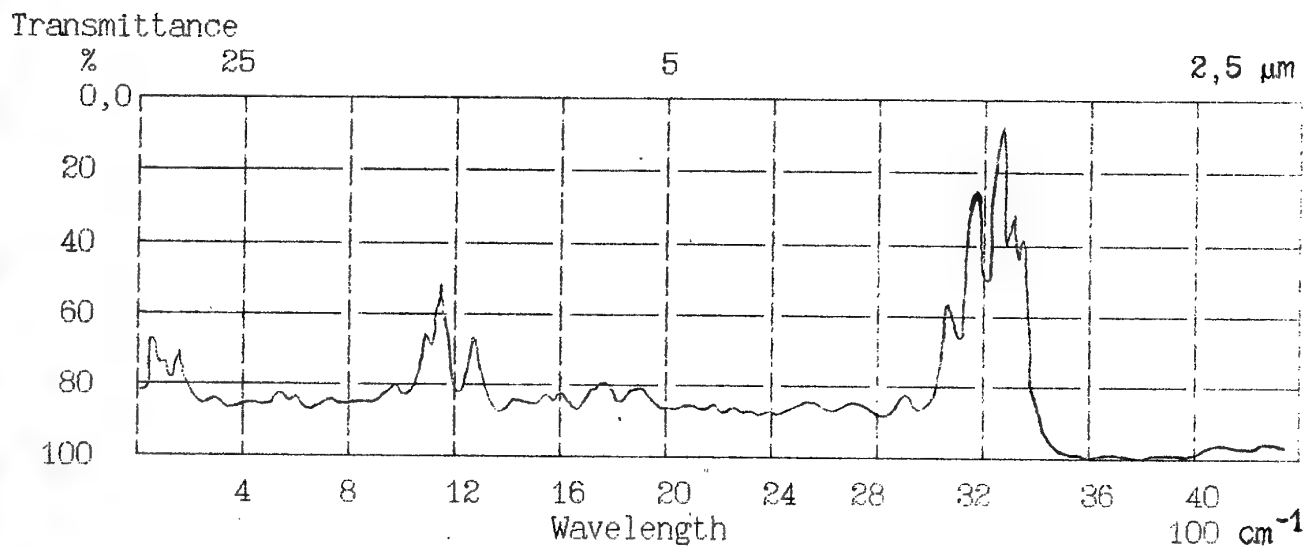


Fig. 65 IR Absorption spectrum of C₇₆ toluene solution for 2.5-25 μm band.

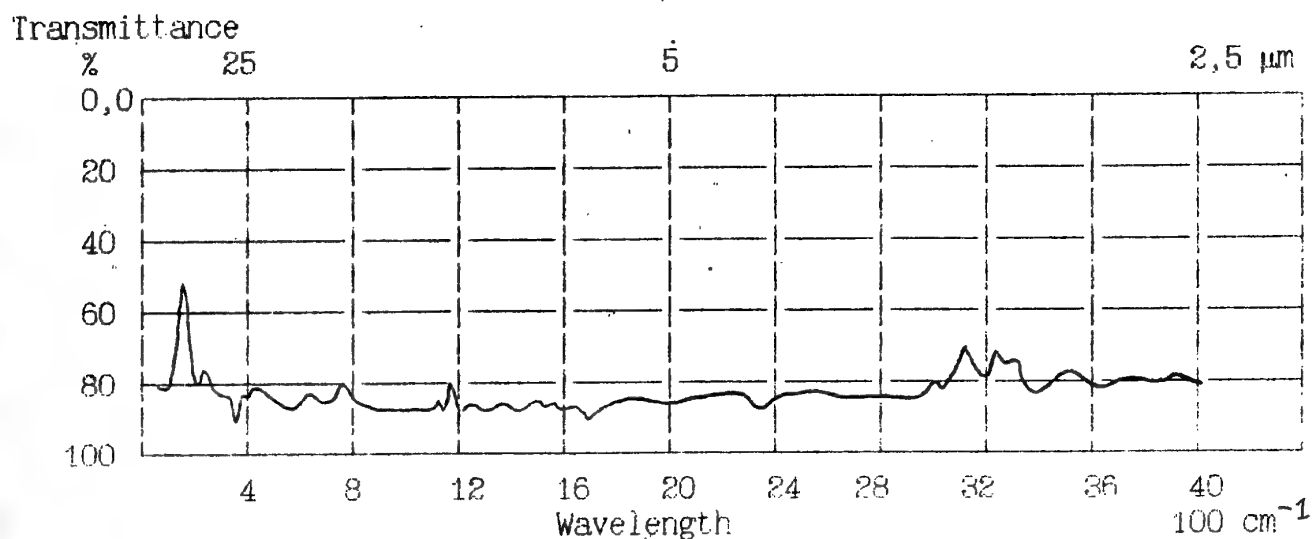


Fig. 66 Absorption spectrum of C₆₀ film (0.2 μm thickness) on a silicon substrate for 2.5 - 25 μm band.

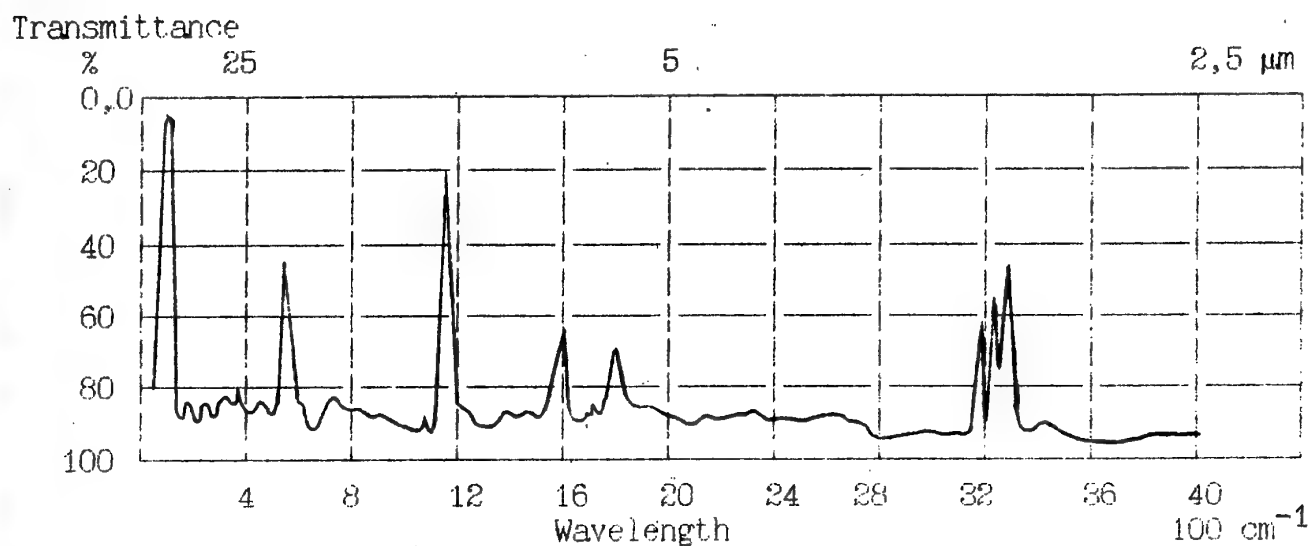


Fig. 67 Absorption spectrum of C₆₀ toluene solution (with respect to pure toluene) for 2.5 - 25 μm band.

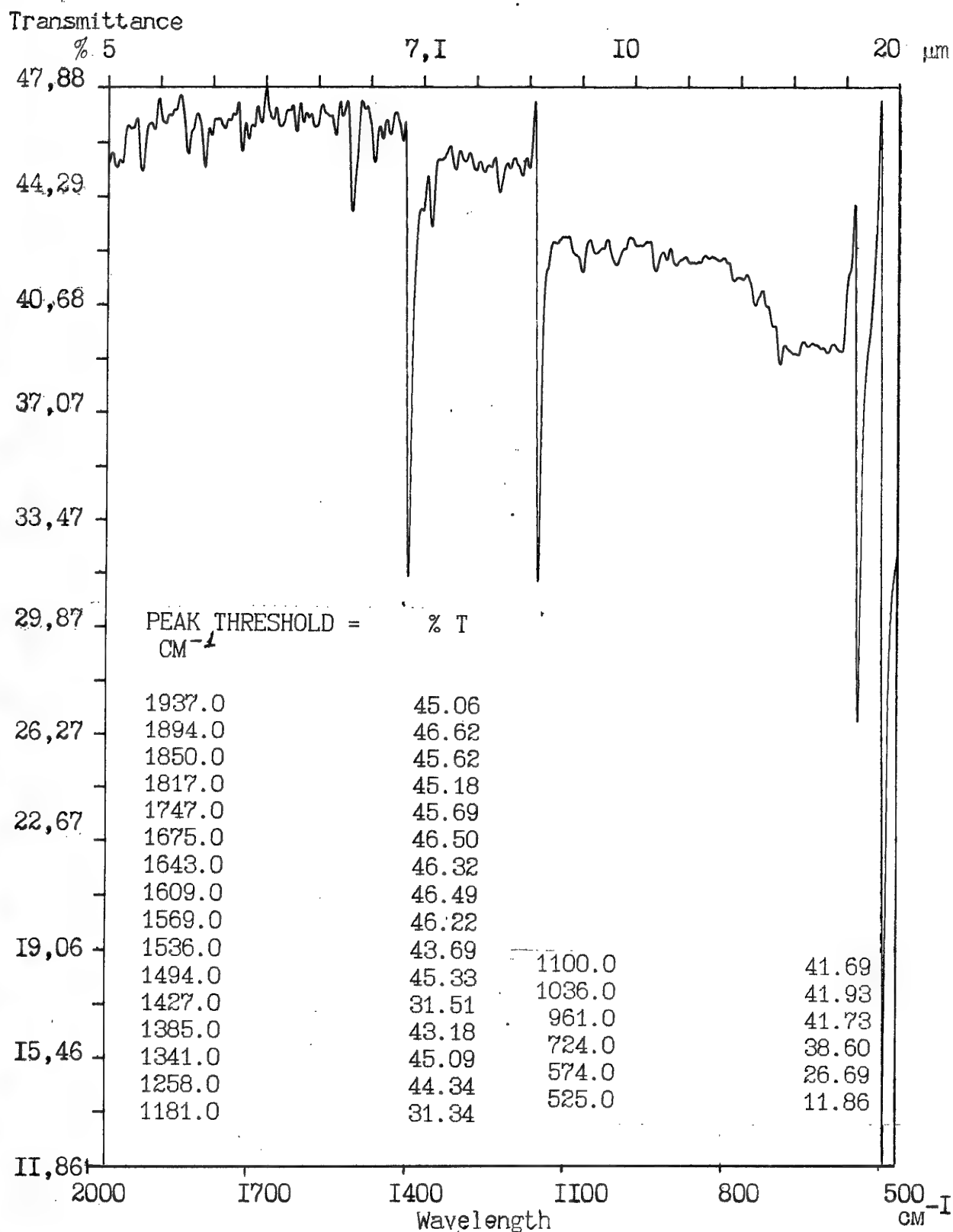


Fig. 68 IR absorption spectrum CsBr mixture.

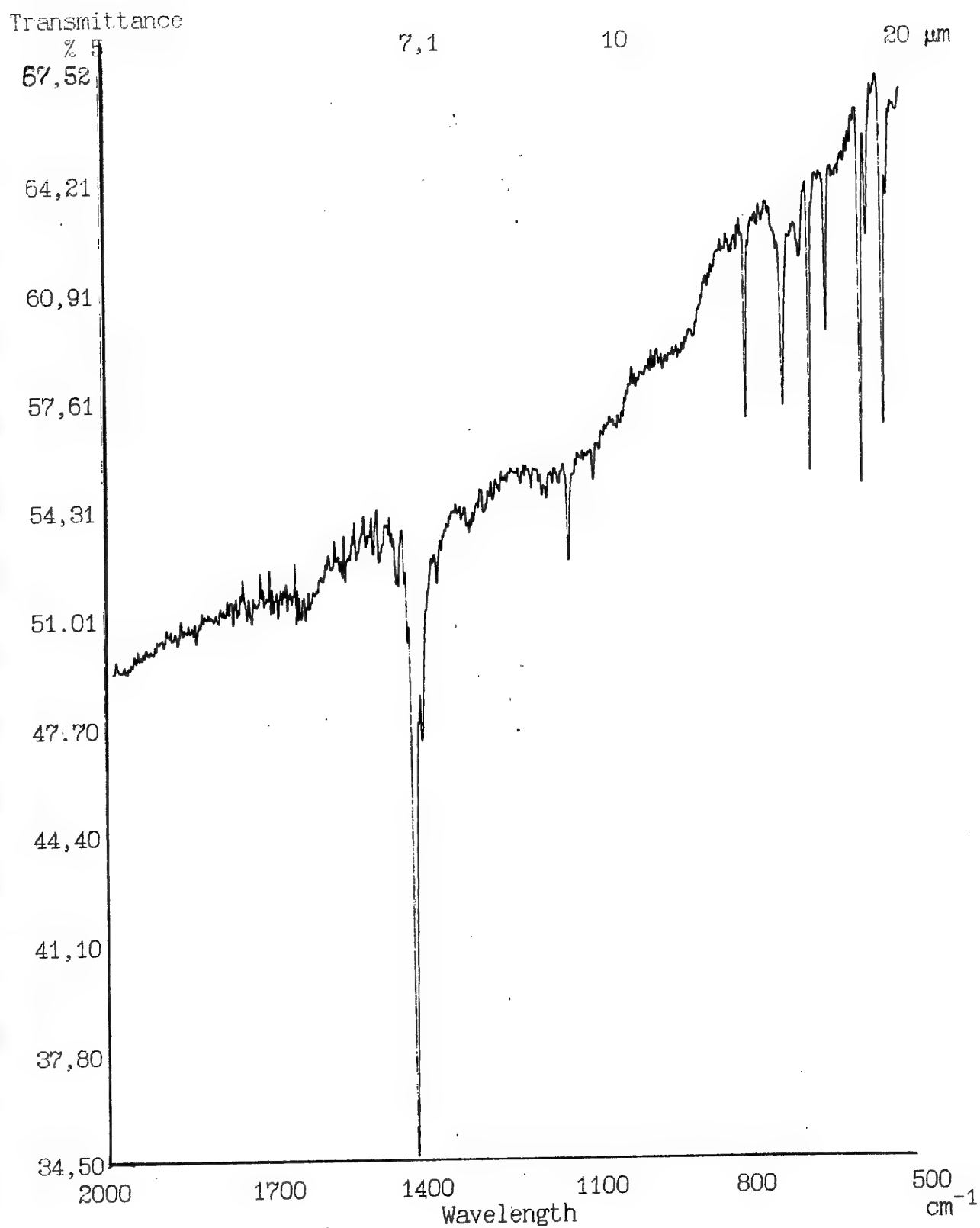


Fig. 69 IR absorption spectrum $\text{C}_{70} + \text{KBr}$ mixture.

Transmittance

% 5

7,1

10

20 μm

98,78

90,58

PEAK THRESHOLD =
CM \sim %

82,39

1628.0	22.17
1459.0	20.99
1428.0	17.59
1182.0	24.96
814.0	71.18
729.0	66.86
664.0	80.05
617.0	82.01
604.0	84.93
577.0	57.82
527.0	18.58

74,19

66,00

57,01

49,62

41,42

33,23

25,03

16,04

2000

1700

1400

1100

800

500

Wavelength.

cm^{-1}

Fig.70 IR absorption spectrum of the first fullerene extraction mixture with KBr.

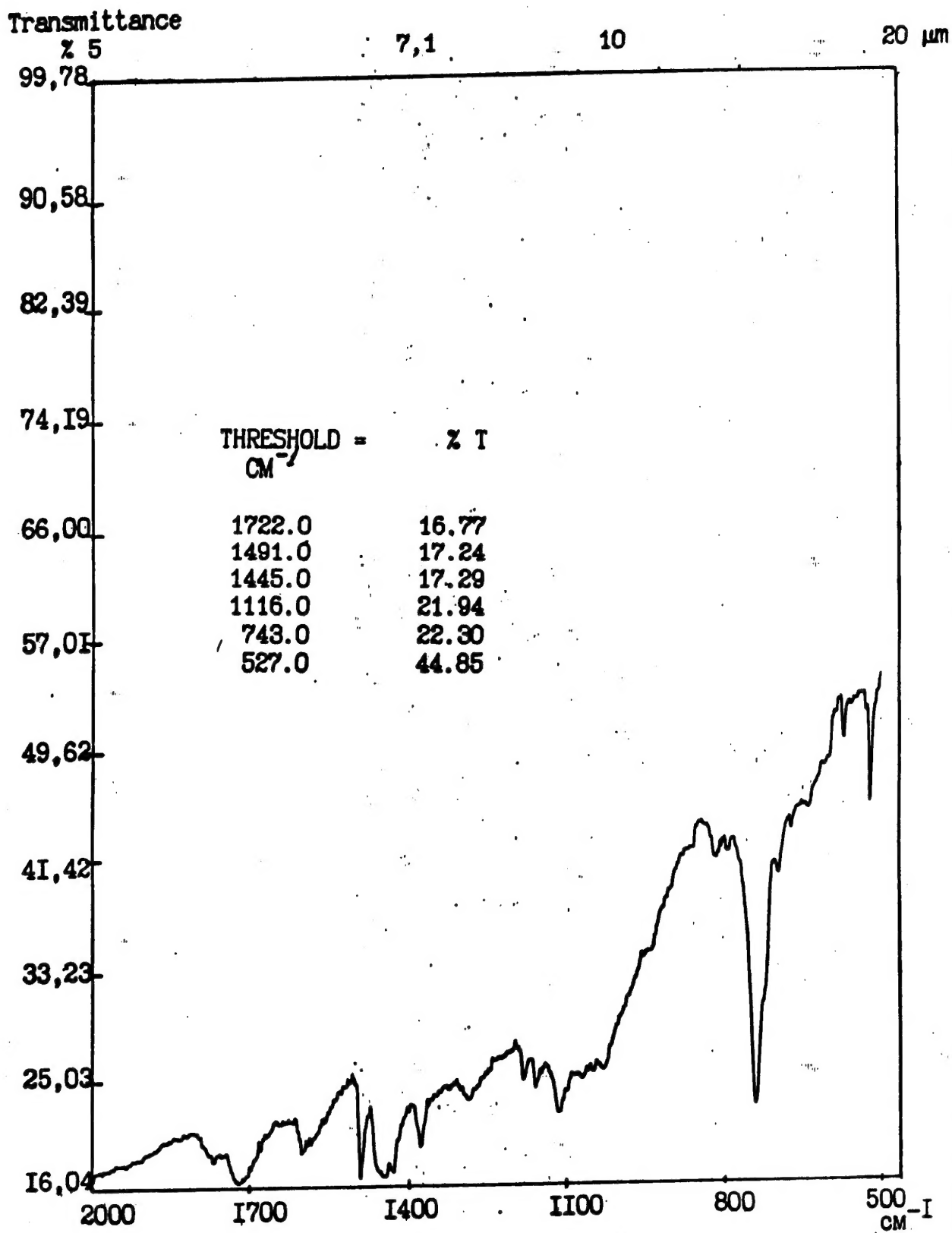


Fig.71 IR absorption spectrum of the sixth fullerene extraction mixture with KBr.

These isomers are inhibited by the contaminants (such as oxygen) as these isomers are more chemically active.

The fullerene C_{76} has absorption at 1000 nm (according to its band gap) therefore the first reason is more probable.

On the base of the absorption experiments we can make the following conclusions:

1. High fullerenes dislocate absorption border into the IR- band.
2. The mixtures of fullerenes contain low fullerenes that diminish the effect of IR- active isomers.

Therefore it is necessary to use the mixtures enriched by individual high fullerenes (or use the semiconductive fullerenes).

REFERENCES TO CHAPTER III

1. H.W.Kroto, J.R.Heath, S.C.O'Brien, R.F.Curl and R.E.Smalley, Nature, 318, 162 (1985).
2. L.D.Lamb, D.R.Huffman, R.K.Workman, S.Howells, T.Chen, D.Sarid and R.F.Ziolo, Science, 1992,
3. W.Kratschmer, K.Fostiropoulus and D.R.Huffman, Chem. Phys. Lett., 170, 167 (1990).
4. P.A.Heiney, J.E.Fisher, A.R.McGhie, W.J.Romanov, A.M.Denenstein, J.P.McCauley Jr., A.B.Smith 111 and D.E.Cox, Phys. Rev. Lett., 66, 2911 (1991).
5. W.I.F.David et al. Nature, 353, 147 (1991).
6. G.Dresselhaus, M.S.Dresselhaus and P.C.Eklund, Phys.Rev. B45 6923 (1992).
7. H.Werner, D.Bublak, U.Gobel, B.Henschke, W.Bensch and R.Schlogl, Angew. Chem. Intern. Ed. Engl., 104, 868 (1992).
8. K.M.Creegan, J.L.Robbins, W.K.Robbins, J.M.Millar, R.D.Sherwood, P.J.Tindall, J.Am.Phys.Sos., 114, 1103 (1992).
9. Y.Elemes, S.K.Silverman, C.Sheu, M.Kao, C.S.Foote, M.M.Alvarez and R.L.Wetten, Angew. Chem. Intern. Ed. Engl., 104, 351 (1992).
10. K.Nakamoto, Infrared spectra of inorganic and coordination compounds (Wiley- Interscience, New York, 1970).

11. B. Chase, N. Herron and E. Holler, J. Phys. Chem. 96, 4262 (1992).
12. M. S. Dresselhaus, G. Dresselhaus and R. Saito, Phys. Rev. B, 45, 6234 (1992).
13. R. A. Jishi, M. S. Dresselhaus, G. Dresselhaus, K. A. Wang, Ping Zhou, A. M. Rao and P. C. Eklund, Chem. Phys. Lett., 206 (1993)
14. B. J. Nelissen, P. H. M. van Loosdrecht, M. A. Vertheijen, A. van der Avoird and G. Meijer, Chem. Phys. Lett., 207, 343 (1993).

CONCLUSIONS

The general conclusions of this work are:

1. On the base of analysis of experimental results and theoretic researches the phenomenological model of charge carrier generation sub action of the irradiation is developed and the carrier transport is discussed in thin film photodevices. A possibility of realization is discussed of the IR-sensitive devices on the base of high fullerenes or doped fullerenes. The study of Shottky transition and heterojunction with polymers is proposed for realization of photosensitive properties of fullerenes to the full extent.

2. On the base of the extended Huckel model, the numeric calculations of electron structure of high fullerenes and the search of isomers with defined band gap are made. The fullerenes with n more than 100 have isomers with narrow band gap.

3. On the base of absorption experiments we can conclude that:

A. High fullerenes dislocate absorption border into the IR- band.

B. The mixtures of fullerenes contain low fullerenes that diminish the effect of IR- active isomers.

On the base of this study we confirm the possibility of obtaining the photoresponse in the fullerene device for near IR-band.